JEM Journal of Experimental Medicine

ARTICLE

TIE2 links MEKK3–KLF2/4 and PI3K signaling in cerebral cavernous malformation

Lun Li[1,2], Marco Castro[3,4], Hiroki Hongo[1,5], Jian Ren[1,6], Robert Shenkar[7], Rashad Jabarkheel[1,2], Siqi Gao[1], Sweta Narayan[1], Maxwell Frankfurter[1], Alan T. Tang[1], Jisheng Yang[1], Mei Chen[1], Jenna Bockman[1], Patricia Mericko-Ishizuka[1], Roberto Alcazar[7], Georgio Sader[7], Javed Iqbal[7], Serena Kinkade[7], Rhonda Lightle[7], Andrew K. Ressler[8], Xianghu Qu[9], H. Scott Baldwin[9], Douglas A. Marchuk[8], Issam A. Awad[7], Jan-Karl Burkhardt[2], Michael Potente[3,4], and Mark L. Kahn[1]

Cerebral cavernous malformations (CCMs) are vascular lesions in the central nervous system that can cause strokes and seizures. Aggressive CCM growth follows an endothelial cell two-hit mechanism in which enhanced MEKK3–KLF2/4 signaling stimulates PI3K signaling, but how these pathways are linked has been undefined. Here, we use human CCM specimens, two mouse models of CCM disease, and primary human endothelial cells to examine the roles of the major endothelial growth factor receptors, VEGFR2 and TIE2. We find no evidence of augmented VEGFR2 signaling in CCM lesions, and neither genetic nor pharmacologic blockade of VEGFR2 reduced CCM formation in mouse models. Instead, we observe markedly increased phospho-TIE2 levels in human and mouse CCM lesions, MEKK3–KLF2/4-driven induction of TIE2 receptor expression, and almost complete rescue of CCM formation following genetic or pharmacologic TIE2 blockade in mouse models. Our studies identify TIE2 as the molecular link between the MEKK3–KLF2/4 and PI3K signaling pathways during CCM formation and suggest that targeting TIE2 may be an effective means to treat human CCM disease.

Introduction

Cerebral cavernous malformations (CCMs) are vascular malformations that arise from venules and veins specifically in the central nervous system (CNS). They are thin-walled and fragile, and hemorrhage is a common complication, causing of stroke, seizures, and neurological deficits. Genetic studies in both humans and mouse models have demonstrated that CCM lesions may arise following endothelial cell loss-of-function (LOF) mutations in one of three genes encoding the CCM complex, including Krev interaction trapped protein 1 (*KRIT1*), *CCM2*, or programmed cell death protein 10 (*PDCD10*). The CCM complex binds and suppresses MEKK3, a MAPK known to respond to both inflammatory signals and fluid shear forces, and activating mutations in MEKK3, encoded by the *MAP3K3* gene, may also cause CCMs. MEKK3 signaling drives increased expression of the related transcription factors KLF2 and KLF4 that are considered the final effectors of this pathway. Clinically, CCMs may arise in a multi-lesion, familial pattern that reflects the presence of a germline CCM gene LOF mutation or, more commonly, in a sporadic manner as a single lesion. Recent studies by our group and others have shown that most rapidly growing CCMs harbor a gain-of-function mutation in *PIK3CA*, the gene encoding the PI3K enzymatic unit, similar to those demonstrated to support the dysregulated growth of tumor cells (Ren et al., 2021; Li et al., 2023; Peyre et al., 2021; Hong et al., 2021). The importance of this two-hit mechanism has been demonstrated in the adult mouse brain, where loss of CCM function or gain of *PIK3CA* function alone are not sufficient to confer lesions, but the combination of the two reproduces human CCM formation (Ren et al., 2021; Li et al., 2023).

An outstanding question to emerge from these recent studies is how gain of MEKK3–KLF2/4 signaling synergizes with gain of PI3K signaling to drive lesion formation. A clue to this question lies in the observation that in the neonatal mouse model—in which endothelial loss of CCM function is sufficient to confer hindbrain CCMs—lesional endothelial cells exhibit markedly high levels of phospho-S6, a marker for mTOR signaling, consistent with elevated PI3K signaling (Li et al., 2023; Ren et al.,

---

[1]Cardiovascular Institute and Department of Medicine, Perelman School of Medicine, University of Pennsylvania, Philadelphia, PA, USA; [2]Department of Neurosurgery, Perelman School of Medicine, Hospital of the University of Pennsylvania, University of Pennsylvania, Philadelphia, PA, USA; [3]Angiogenesis & Metabolism Laboratory, Center of Vascular Biomedicine, Berlin Institute of Health at Charité - Universitätsmedizin Berlin, Berlin, Germany; [4]Max Delbrück Center for Molecular Medicine in the Helmholtz Association, Berlin, Germany; [5]Department of Neurosurgery, Faculty of Medicine, The University of Tokyo, Tokyo, Japan; [6]Department of Neurosurgery, Xuanwu Hospital, China International Neuroscience Institute, National Center for Neurological Disorders, Capital Medical University, Beijing, China; [7]Department of Surgery, Neurovascular Surgery Program, Section of Neurosurgery, Medicine and Biological Sciences, The University of Chicago, Chicago, IL, USA; [8]Department of Molecular Genetics and Microbiology, School of Medicine, Duke University, Durham, NC, USA; [9]Division of Pediatrics Cardiology, Department of Cell and Developmental Biology, Vanderbilt University, Nashville, TN, USA.

Correspondence to Mark L. Kahn: markkahn@pennmedicine.upenn.edu.

Rockefeller University Press
J. Exp. Med. 2026 Vol. 223 No. 5 e20251374

https://doi.org/10.1084/jem.20251374

2021). The significance of this observation and the role of PI3K signaling downstream of MEKK3–KLF2/4 signaling are revealed by the observation that such neonatal CCM lesions can be almost entirely blocked by the mTOR antagonist rapamycin (Li et al., 2023; Ren et al., 2021). These studies support a mechanism in which augmented MEKK3–KLF2/4 signaling drives lesion growth primarily by increasing PI3K–mTOR signaling in endothelial cells. However, the molecular mechanism by which augmented MEKK3–KLF2/4 function confers increased PI3K–mTOR signaling has remained unclear. Addressing this question also has potentially important translational implications: inhibition of PI3K–mTOR signaling with agents such as rapamycin is highly effective in mouse models that require only several days of treatment (Li et al., 2023), but these agents are less ideal in clinical practice where patients must endure significant side effects in highly proliferative organs such as the skin and hematopoietic system. Determining how endothelial cells augment PI3K signaling downstream of MEKK3–KLF2/4 signaling could identify a more endothelial cell–specific therapeutic strategy for chronic suppression of lesion growth.

In the present study, we have tested whether MEKK3–KLF2/4 signaling stimulates the PI3K pathway through classic endothelial growth factor receptors known to couple to that pathway. Analysis of human CCM lesions, neonatal and adult mouse CCM models, and *in vitro* studies of cultured endothelial cells revealed no significant role for VEGF signaling in this mechanism. Instead, we find that signaling by the angiopoietin receptor TIE2 (encoded by the *TEK* gene) was enhanced in endothelial cells lining human CCMs, those lining CCMs in neonatal and adult mouse models, and in cultured CCM-deficient endothelial cells. Consistent with these findings, pharmacologic or genetic blockade of VEGF signaling had no impact on CCM lesion growth in mouse models, but genetic loss of TIE2 or treatment with the TIE2 kinase inhibitor rebastinib almost completely blocked lesion formation in mouse models. These findings identify angiopoietin-TIE2 signaling as a crucial link between the MEKK3–KLF2/4 and PI3K signaling pathways and suggest that pharmacologic blockade of TIE2 may provide an endothelial cell–centered approach for chronic suppression of CCM disease with fewer side effects than systemic PI3K–mTOR inhibition.

Results

Signaling by TIE2 but not VEGFR2 is increased in human CCM endothelium

Human CCM lesions arise following an endothelial cell CCM gene LOF mutation or a *MAP3K3* gain-of-function mutation that increases KLF2/4 expression and PI3K–mTOR signaling, thereby fueling endothelial cell proliferation and lesion growth. How these two pathways are linked has been unclear. We hypothesized that MEKK3–KLF2/4 signaling might stimulate PI3K signals through increased activity of major endothelial cell growth factors such as VEGFR2 and TIE2 that are known to couple to this pathway and drive endothelial cell proliferation. Prior studies have reported that pharmacologic inhibition of VEGFR2 (DiStefano and Glading, 2020) and TIE2 (Zhou et al., 2021) can reduce CCM growth in the neonatal mouse models, but these findings are difficult to interpret because (1) the small molecular kinase antagonists used are not highly receptor specific, and (2) CCM formation in the neonatal brain requires a high level of angiogenic activity and therefore could be blocked by agents that target the angiogenic activity independent of the MEKK3–KLF2/4 pathway.

To circumvent these limitations, we first examined whether CCM lesions that come to clinical attention in adult human patients exhibit significant changes in endothelial cell phospho-VEGFR2 (pVEGFR2) or phospho-TIE2 (pTIE2), biochemical markers for receptor activation that can be assessed using site-specific antibodies. Immunostaining was performed on histologic sections of four human cavernous malformations freshly resected from adult patients, ages 20–73, at the Hospital of the University of Pennsylvania, Philadelphia, PA, USA. One of these lesions (CCM patient #6, Fig. S1 A) arose in a patient with a family history of CCM disease harboring a germline *KRIT1* mutation, i.e., a familial CCM lesion, while the others were isolated sporadic lesions. Although these lesions were not genotyped, our past studies suggest that most sporadic CCM lesions contain endothelial cells with either two CCM gene LOF mutations or an *MAP3K3* I441M mutation in addition to a *PIK3CA* gain-of-function mutation (Ren et al., 2021). As previously described, CCM vascular lesions were readily identified as large, thin-walled, blood-filled vascular structures (Fig. 1 A and Fig. S1 A). Immunostaining identified a thin layer of CD31 (PECAM1)-positive endothelium around bright, autofluorescent red blood cell pools in CCM lesions and smaller vessels in control brain tissue (Fig. 1 A and Fig. S1 A). Anti-VEGFR2 antibodies detected the receptor in CD31$^+$ cells, but antibodies specific for VEGFR2 phospho-tyrosine 951 (anti-pVEGFR2$^{\mathrm{Tyr951}}$) or phospho-tyrosine 1175 (anti-pVEGFR2$^{\mathrm{Tyr1175}}$), required for VEGFR2 kinase domain activation and PI3K signaling, respectively, did not label CCM lesional endothelium (Fig. 1 A and Fig. S1 A). In contrast, both phospho-epitopes were reliably detected in human glioblastoma samples, where robust angiogenic signaling and VEGFR2 phosphorylation are evident in tumor-associated brain vessels (Lee et al., 2023) (Fig. S1, B–F). Conversely, CCM lesional endothelium stained strongly using both anti-TIE2 antibodies and anti–phospho-tyrosine 992 TIE2 (the autophosphorylation site in the receptor's activation loop) (Fig. 1 A and Fig. S1 A). A similar immunostaining pattern was observed in a genotype-identified CCM case (*PIK3CA*$^{\mathrm{H1047R}}$ with a somatic *CCM2* mutation), as previously characterized in Ren et al. (2021), in which pTIE2, but not pVEGFR2, was detected at the lesional endothelium (Fig. S1 G). VEGFR2 phospho-tyrosine 951 or 1,175 and TIE2 phospho-tyrosine 992 were not detected in the endothelium of control brain (Fig. 1 A and Fig. S1 A). Quantitative analysis of the fluorescent signal at lesional endothelium using these antibodies confirmed a marked increase in pTIE2 but no change in pVEGFR2 staining (Fig. 1, B–D). These studies suggested that human CCM lesions exhibit increased TIE2 but not VEGFR2 receptor signaling.

TIE2 signaling is an early event in CCM lesion formation in mature mice

To study CCM disease pathogenesis in an animal model that more closely resembles the two-hit mechanism present in most

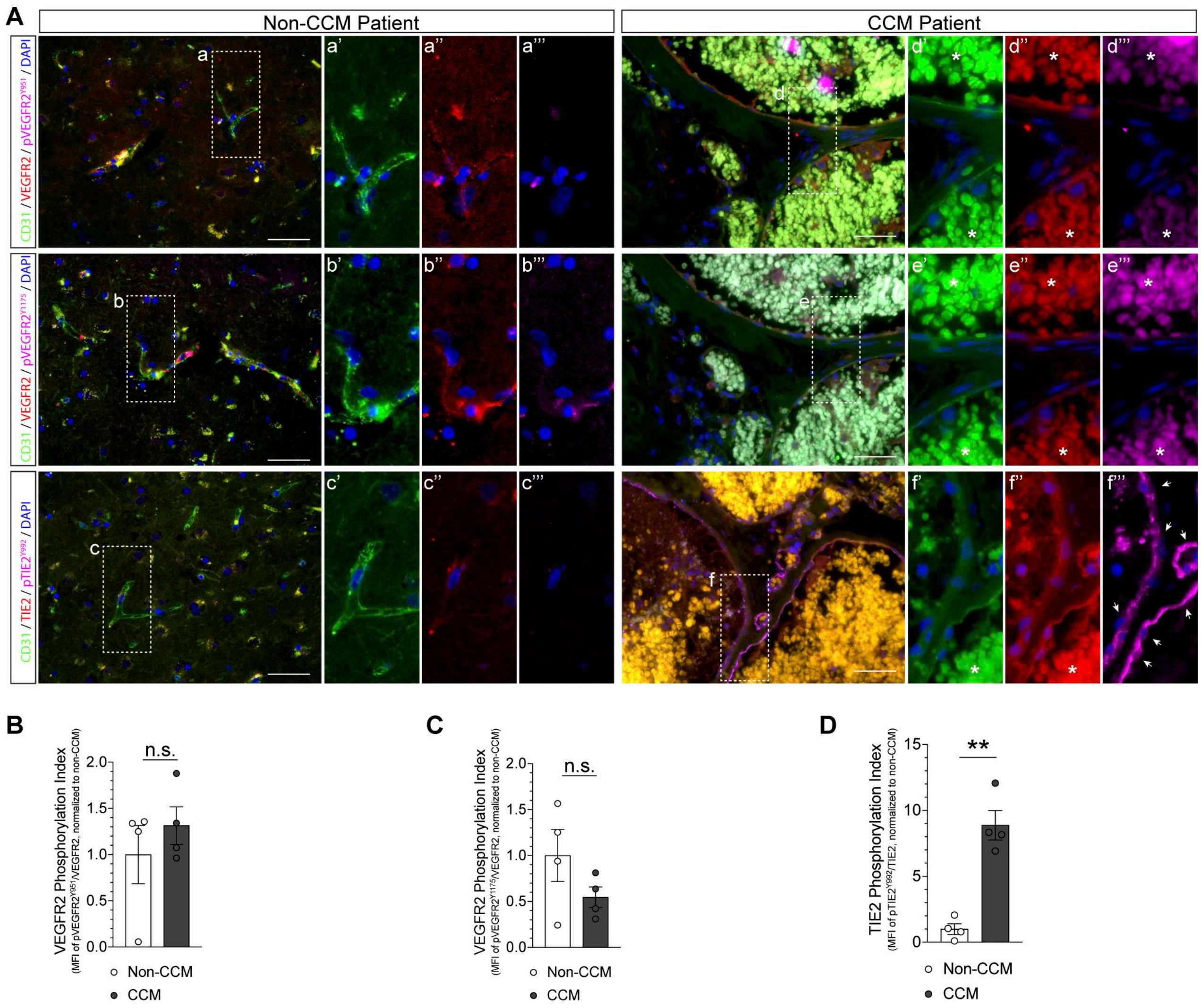

Figure 1. **Detection of pTIE2 but not pVEGFR2 in human CCM lesional endothelium. (A)** Representative images showing immunostaining for CD31, VEGFR2, pVEGFR2, and TIE2, pTIE2, with DAPI counterstaining in freshly resected human CCM specimens and non-CCM human brain tissue. The boxed regions in the lower-magnification images are shown at higher magnification on the right. Arrows indicate pTIE2-positive endothelial cells lining CCM lesions. Asterisks indicate autofluorescence emitted from lumenal red blood cells. Scale bar: 100 µm. **(B–D)** Quantification of MFI of (D) pVEGFR2^{Y951}, (E) pVEGFR2^{Y1175}, and (F) pTIE2^{Y992}, normalized to total VEGFR2 and TIE2, respectively, as compared with endothelium in non-CCM brain tissue. *N* = 4 human samples in each group were analyzed and quantified. Data shown are means ± SEM. **P <0.01 by unpaired two-tailed Welch *t* test. No statistically significant (n.s.) differences are observed in (B) P = 0.4409 and (C) P = 0.2107.

human CCMs, our lab has recently developed a mouse model in which CCM LOF and PI3K gain-of-function are conferred in a local manner in the brain of adult animals through injection of adeno-associated virus (AAV)-Cre using a cranial window (Ren et al., 2021; Li et al., 2023) (Fig. 2 A). This model recapitulates the key morphologic features of human CCM disease, including peri-lesional hemorrhage. It also permits observation of lesion growth in live animals that can be used to assess the impact of genetic and pharmacologic interventions (Ren et al., 2021; Li et al., 2023) (Fig. 2 B). To further assess VEGFR2 and TIE2 signaling, we therefore assessed phospho-tyrosine staining in mature and nascent lesions using this mouse model. Immunostaining of CCM lesions and control tissue from the contralateral brain of the same animals harvested 155 days after injection of AAV-Cre revealed no change in pVEGFR2 at either Y951 or Y1175 in CCM lesion endothelium (Fig. 2, C–E). In contrast, a marked, approximately ninefold increase in pTIE2 at Y992 was observed in CCM lesional endothelium compared with control (Fig. 2, C and F).

These studies and those described above using freshly excised human CCM tissue demonstrated that TIE2 activity was markedly elevated in mature CCM lesions. However, since numerous studies have documented secondary inflammatory changes associated with CCM formation (Lai et al., 2022; Shi et al., 2009), whether activation of TIE2 signaling was a primary or secondary event was not clear. To address this question, we next examined pVEGFR2 and pTIE2 staining 7 days after injection of AAV-Cre, a time point prior to the formation of visible vascular malformations. To identify the Cre-expressing region of the brain prior to lesion formation, we used animals that carried a tdTomato Cre reporter (Ai14) in addition to floxed *Krit1* and

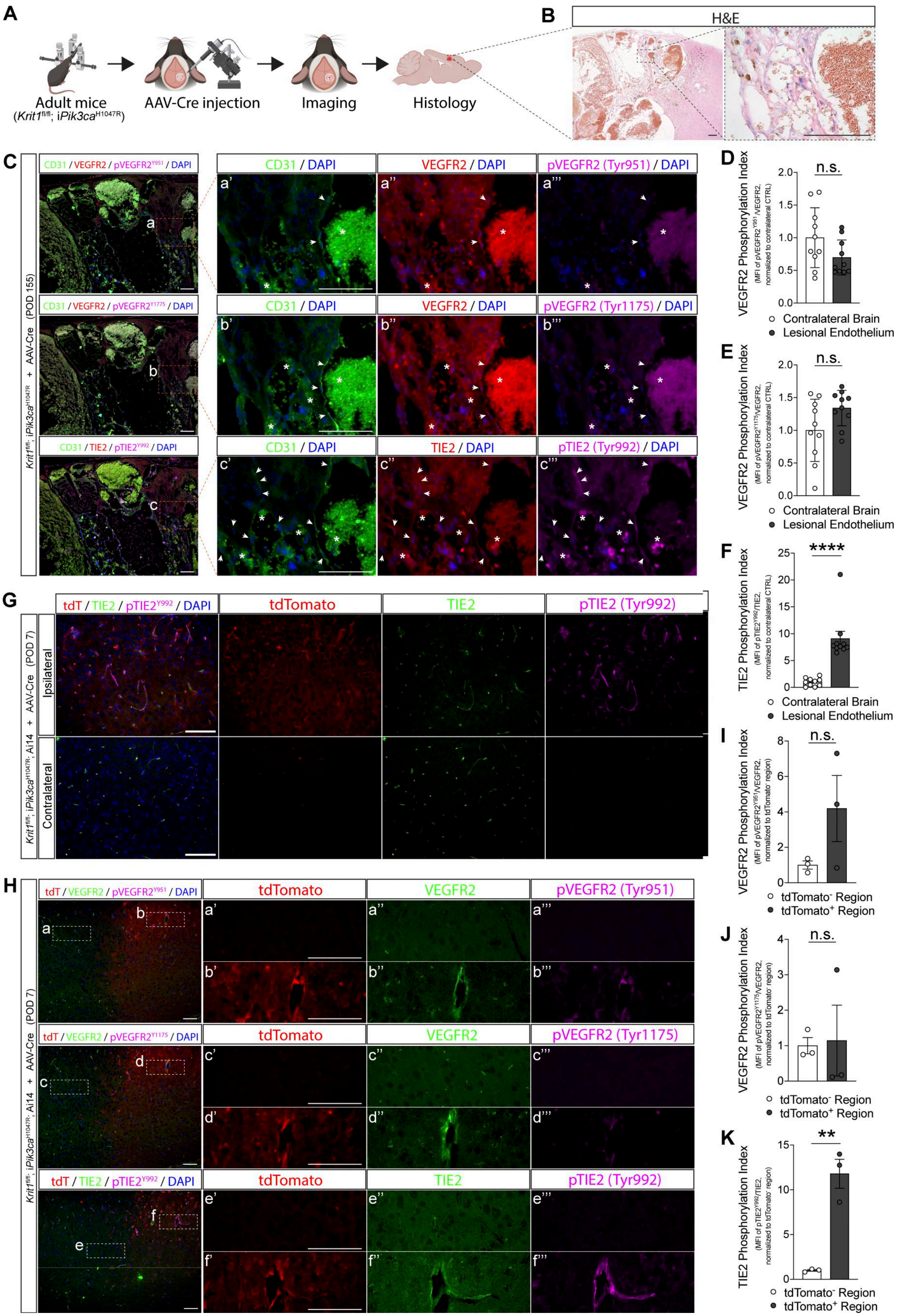

Figure 2. **TIE2, but not VEGFR2, is activated at the CCM lesional endothelium in adult mouse brain. (A)** Schematic representation of the adult inducible CCM model incorporating both loss of CCM function and gain of PI3K function. *Krit1*$^{fl/fl}$; *iPik3ca*^{H1047R} mice between age 8–10 wk underwent craniotomy and

received AAV-Cre injections to induce focal Cre-mediated *Krit1* deletion and *Pik3ca*^{H1047R} overexpression in the cerebral cortex below a cranial window. **(B)** Representative images of H&E staining revealing a classic popcorn lesion appearance (left) with enlarged vasculature ("caverns") and peri-lesional hemosiderin indicative of hemorrhage in older lesions (right). **(C)** Representative images showing immunostaining for CD31, VEGFR2, pVEGFR2, TIE2, and pTIE2, with DAPI counterstaining in a mouse CCM harvested on POD 155. The boxed regions, a–c, are shown at higher magnification in a'–a''' to c'–c''', respectively. **(D–F)** Quantification of MFI of (D) pVEGFR2^{Y951}, (E) pVEGFR2^{Y1175}, and (F) pTIE2^{Y992} normalized to total (D and E) VEGFR2 and (F) TIE2, respectively, compared with vasculature in the contralateral, uninjected side of the brain. A total of 10 regions in each group were measured and quantified. **(G and H)** Representative images showing immunostaining for tdTomato, VEGFR2, pVEGFR2, TIE2, and pTIE2, with DAPI counterstaining in brains harvested on POD 7. The boxed regions, a–f, are shown at higher magnification in a'–a''' to f'–f''', respectively. **(I–K)** Quantification of MFI of (I) pVEGFR2^{Y951}, (J) pVEGFR2^{Y1175}, and (K) pTIE2^{Y992} normalized to total (I and J) VEGFR2 and (K) TIE2, respectively, as compared with the tdTomato-negative regions. A total of three mice in each group were measured and quantified. Arrows indicate pVEGFR2- or pTIE2-positive endothelial cells at the CCM lesions. Asterisks indicate autofluorescence emitted from lumenal red blood cells. Scale bar: 100 µm. Data shown are means ± SEM. $^{**}P < 0.01$ and $^{****}P < 0.0001$ by two-tailed Mann–Whitney *U* test (D–F) and unpaired two-tailed Welch *t* test (I–K). No statistically significant (n.s.) differences are observed in (D) P = 0.1839, (E) P = 0.1051, (I) P = 0.1652, and (J) P = 0.8967.

Cre-activated *Pik3ca*^{H1047R} alleles. Immunostaining revealed no difference in pVEGFR2 between the tdTomato-positive and tdTomato-negative regions of the injected brain, but pTIE2 was increased >10-fold in TIE2-positive endothelial cells within the tdTomato-positive zone compared with either adjacent tdTomato-negative vasculature or vasculature in the uninjected contralateral half of the brain (Fig. 2, G–K). The increased pTIE2 is not attributable to craniotomy- or stereotactic injection–induced focal injuries, nor to regional inflammation from AAV transduction (Fig. S2, A and B). These findings reveal strong and specific upregulation of TIE2 signaling that is present from an early time point during CCM lesion formation *in vivo*, consistent with a primary and causal mechanism.

Genetic deletion of *Kdr* does not block CCM formation in the neonatal or adult mouse models

Given the central role played by VEGF signaling in vascular growth and prior studies suggesting that pharmacologic inhibition of VEGF signaling reduces CCM lesion growth in mice (DiStefano and Glading, 2020), we next used genetic deletion of *Kdr* (encoding VEGFR2) to test its requirement during CCM formation in mice. Adult *Krit1*$^{fl/fl}$; *iPik3ca*^{H1047R} and *Krit1*$^{fl/fl}$; *iPik3ca*^{H1047R}; *Kdr*$^{fl/fl}$ mice aged 8–10 wk underwent craniotomy, followed by AAV-Cre injection (Fig. 3 A). To ensure loss of VEGFR2, immunostaining was performed using mice that also carried an Ai14 Cre reporter allele to identify Cre-expressing and neighboring Cre-negative brain tissue. At postoperative day (POD) 7, ∼80% of CD31$^+$ endothelial cells in the tdTomato-positive zone (CD31$^+$/Ai14$^+$) lacked detectable VEGFR2 immunofluorescent signal compared with CD31$^+$ endothelium in neighboring tdTomato-negative brain tissue (Fig. 3, B and C). Time-lapse microscopic images captured through the cranial window from POD 7 to POD 21 showed no visible differences in lesion onset days or growth rate between the two groups of mice until POD 21 when tissues were harvested (Fig. 3 D). Although this model results in significant variability in lesion growth, after sacrifice on POD 21, CCM lesion size did not differ significantly between animals with and without VEGFR2 measured using quantitative contrast-enhanced microcomputed tomography (microCT) (Girard et al., 2016) (Fig. 3, E and F; and Fig. S2 C). Histologic analysis revealed that lesions in *Krit1*$^{fl/fl}$; *iPik3ca*^{H1047R}; *Kdr*$^{fl/fl}$ mice exhibited typical CCM pathology, with evidence of chronic hemorrhagic events observed in this model (Fig. S2 D).

In the neonatal CCM model driven exclusively by loss of CCM function, CCMs arise exclusively in angiogenic regions of the postnatal brain such as the hindbrain and retina (Chan et al., 2011; Boulday et al., 2011)—consistent with a requirement for endogenous angiogenic signals. Some human familial CCMs are also thought to arise during brain development. Thus, it was possible that VEGFR2 might be required for CCM lesion formation that takes place during developmental angiogenic periods but not in fully mature animals. To address the functional requirement for VEGFR2 using the mouse neonatal CCM model that does not require gain of PI3K function, we intragastrically administered a single dose of 4-hydroxytamoxifen (4-OHT) to postnatal day 1 (P1) *Cdh5-Cre*^{ERT2}; *Krit1*$^{fl/fl}$; *Kdr*$^{fl/fl}$ and control littermate animals. We observed a significant loss of VEGFR2 protein, measured both by western blotting of total cerebellum lysate (that also contains VEGFR2$^+$ neurons) and immunostaining of hindbrain tissue sections using antibodies for CD31 and VEGFR2 (Fig. 3, G–K). Analysis of pVEGFR2 in tissue sections revealed reduced rather than increased pVEGFR2 in *Cdh5-Cre*^{ERT2}; *Krit1*$^{fl/fl}$ brains (Fig. 3 L), suggesting that loss of CCM function lowers rather than augments VEGFR2 signaling. Consistent with its role in vascular growth, the brain size of *Cdh5-Cre*^{ERT2}; *Krit1*$^{fl/fl}$; *Kdr*$^{fl/fl}$ animals harvested on P11 was smaller than littermate *Cdh5-Cre*^{ERT2}; *Krit1*$^{fl/fl}$; *Kdr*$^{fl/+}$ controls (Fig. 3, M and O). However, loss of VEGFR2 did not significantly diminish CCM formation in the hindbrain measured using microCT on P11 (Fig. 3, M and N) but instead led to the appearance of new lesions in the neonatal forebrain, a region that does not typically develop CCM lesions in neonatal brains with *Krit1* LOF alone (Fig. S3). These functional studies are consistent with our finding that CCM lesional endothelium in mice and humans does not exhibit pVEGFR2, suggesting that VEGFR2 is neither a driver of CCM formation nor the link by which MEKK3–KLF2/4 signaling activates PI3K.

Genetic deletion of *Tek* prevents CCM formation in the neonatal and adult mouse models

The studies described above suggested that TIE2 might play an important functional role in CCM formation downstream of augmented MEKK3–KLF2/4 signaling. To functionally test this hypothesis, we explored whether deletion of *Tek* (encoding TIE2) impacts lesion growth conferred by KRIT1 LOF and PI3K gain-of-function using the adult cranial window model. *Krit1*$^{fl/fl}$; *iPik3ca*^{H1047R} and *Krit1*$^{fl/fl}$; *iPik3ca*^{H1047R}; *Tek*$^{fl/fl}$ mice aged 8–10 wk underwent craniotomy, followed by AAV-Cre injection (Fig. 4 A). At POD 7, ∼75% of CD31$^+$ endothelial cells in the tdTomato-positive zone

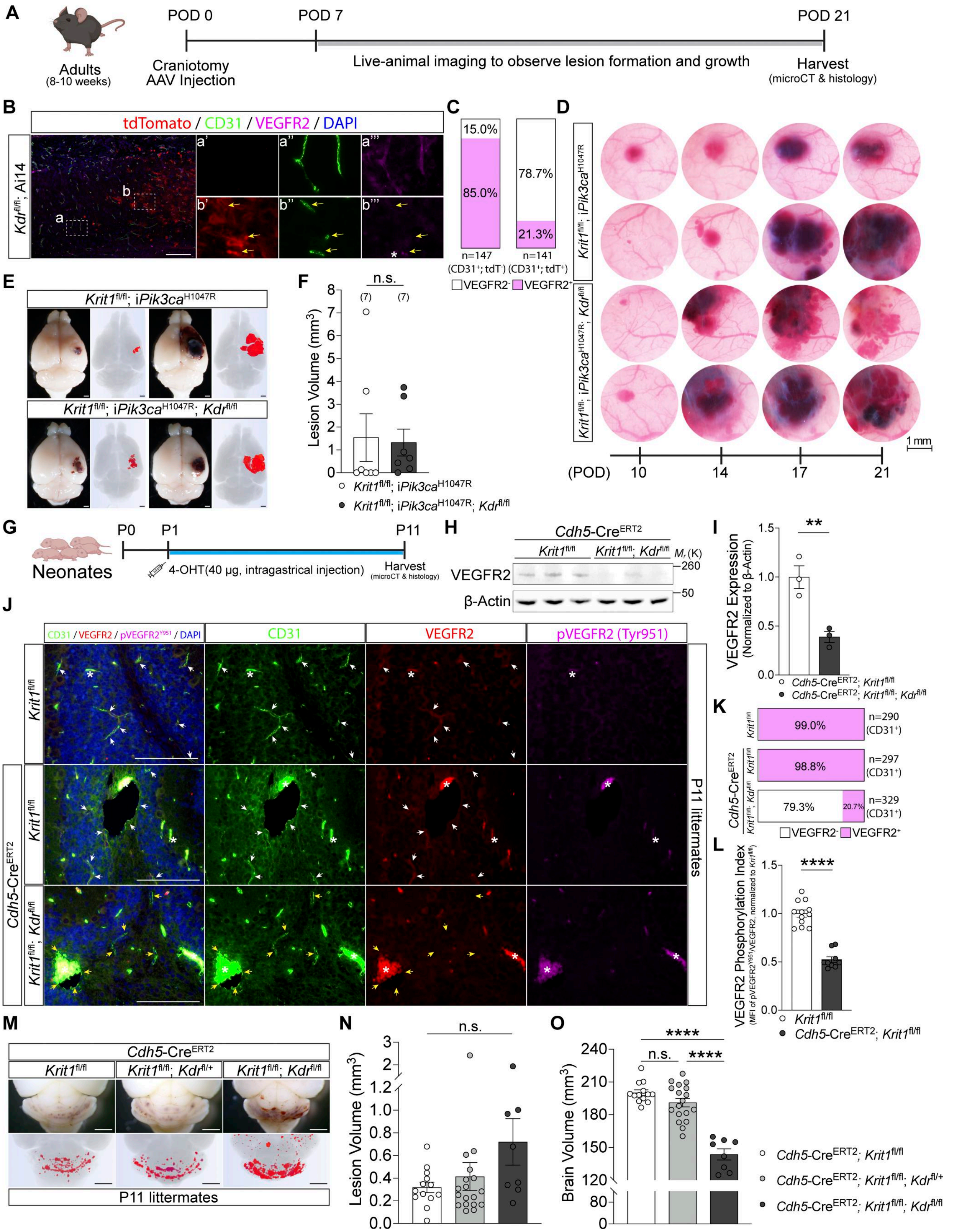

Figure 3. **Endothelial deletion of *Kdr* does not prevent CCM formation in the adult or neonatal mouse model. (A)** Schematic representation of adult *Krit1*$^{\mathrm{fl/fl}}$; *iPik3ca*$^{\mathrm{H1047R}}$ mice or *Krit1*$^{\mathrm{fl/fl}}$; *iPik3ca*$^{\mathrm{H1047R}}$; *Kdr*$^{\mathrm{fl/fl}}$ mice, aged 8–10 wk, underwent craniotomy and received focal AAV-Cre injections. Live-animal

microscopic images were captured through the cranial window from POD 7 to POD 21 to observe lesion formation and growth. **(B)** Representative images showing immunostaining for tdTomato, CD31, and VEGFR2, with DAPI counterstaining in brains harvested from *Kdr*$^{fl/fl}$; Ai14 mice on POD 7. The boxed regions in the tdTomato-negative regions (a) and in the tdTomato-positive regions (b) are shown in a′–a‴ and b′–b‴, respectively, at higher magnification. Yellow arrows indicate CD31-positive but VEGFR2-negative endothelial cells in the tdTomato-positive regions (tdTomato$^+$, CD31$^+$, and VEGFR2$^-$). Scale bar: 100 µm. **(C)** Quantification of VEGFR2-positive (CD31$^+$; VEGFR2$^+$) and VEGFR2-negative (CD31$^+$; VEGFR2$^-$) endothelial cells in both tdTomato-negative and -positive regions. **(D)** Serial of microscopic images through the cranial windows showing CCM growth in either *Krit1*$^{fl/fl}$; *iPik3ca*^{H1047R} or *Krit1*$^{fl/fl}$; *iPik3ca*^{H1047R}; *Kdr*$^{fl/fl}$ mouse brains from POD 10 to POD 21. **(E and F)** Representative visual images (left panels) and microCT renders (right panels) (E), and (F) microCT quantification of CCM lesion volumes in *Krit1*$^{fl/fl}$; *iPik3ca*^{H1047R} ($n = 7$) or *Krit1*$^{fl/fl}$; *iPik3ca*^{H1047R}; *Kdr*$^{fl/fl}$ ($n = 7$) mouse brains harvested on POD 21. The same microCT renders are also shown in Fig. S2 C to provide a comprehensive overview of genotype-dependent effects on lesion burden across the entire study cohort. Scale bar: 1 mm. **(G)** Schematic representation of neonatal induction of *Krit1* deletion with or without *Kdr* deletion. 4-OHT was intragastrically injected on P1, and brains were harvested on P11. **(H)** Immunoblot detection of VEGFR2 in neonatal cerebellum harvested from P11 littermates. β-Actin was used as a loading control. **(I)** Quantification of immunoblotting for VEGFR2 protein level. A total of three paired littermates were measured and quantified. **(J)** Representative images showing immunostaining for CD31, VEGFR2, and pVEGFR2, with DAPI counterstaining in neonatal brains harvested from P11 littermates. White arrows indicate CD31 and VEGFR2 double-positive (CD31$^+$; VEGFR2$^+$) cells and yellow arrows indicate CD31-positive but VEGFR2-negative (CD31$^+$; VEGFR2$^-$) cells at the lesional and non-lesional neonatal cerebellum. Asterisks indicate autofluorescence emitted from lumenal red blood cells. Scale bar: 100 µm. **(K)** Quantification of VEGFR2-positive (CD31$^+$; VEGFR2$^+$) and VEGFR2-negative (CD31$^+$; VEGFR2$^-$) cerebellar endothelial cells. **(L)** Quantification of MFI of pVEGFR2^{Y951} in *Krit1*^{ECKO} (*Cdh5-Cre*^{ERT2}; *Krit1*$^{fl/fl}$) neonatal cerebellum, normalized to total VEGFR2, compared with vasculature in the normal littermate control (*Krit1*$^{fl/fl}$). **(M–O)** Representative visual images (top panels) and microCT renders (bottom panels), and microCT quantification of (N) CCM lesion volumes and (O) total brain volumes in *Cdh5-Cre*^{ERT2}; *Krit1*$^{fl/fl}$ ($n = 13$), *Cdh5-Cre*^{ERT2}; *Krit1*$^{fl/fl}$; *Kdr*$^{fl/+}$ ($n = 18$), and *Cdh5-Cre*^{ERT2}; *Krit1*$^{fl/fl}$; *Kdr*$^{fl/fl}$ ($n = 8$) mouse brains harvested on P11. The same brain specimens and corresponding microCT renders are also shown in Fig. S3 A to provide a global view of the whole brain. Representative images in this panel are presented with emphasis on cerebellar lesions. Scale bar: 1 mm. Data shown are means ± SEM. $^{**}P < 0.01$ and $^{****}P < 0.0001$ by two-tailed Mann–Whitney *U* test (F and L), unpaired two-tailed *t* test (I), and one-way ANOVA, followed by Tukey HSD post hoc test (N and O). No statistically significant (n.s.) differences are observed in (F) $P = 0.3036$, (N) $P = 0.1443$, and (O) $P = 0.1900$. Source data are available for this figure: SourceData F3. Tukey HSD, Tukey's honestly significant difference.

(CD31$^+$/Ai14$^+$) lacked detectable TIE2 immunofluorescent signal compared with CD31$^+$ endothelium in neighboring tdTomato-negative brain tissue (Fig. 4, B and C). Time-lapse microscopic imaging, captured from POD 7 to POD 21, revealed lesion formation at the injection site in most *Krit1*$^{fl/fl}$; *iPik3ca*^{H1047R} animals, but almost no visible lesion formation in *Krit1*$^{fl/fl}$; *iPik3ca*^{H1047R}; *Tek*$^{fl/fl}$ animals (Fig. 4 D). Volumetric measurements of CCM lesions using blinded microCT analysis showed a highly significant reduction in lesion size in brains harvested on POD 21 (Fig. 4, E and F; and Fig. S4 A). Notably, 2 out of 20 brains in the *Krit1*$^{fl/fl}$; *iPik3ca*^{H1047R}; *Tek*$^{fl/fl}$ group exhibited significant CCM lesions on POD 21 (Fig. 4 F; and Fig. S4, B and C), possibly due to failure or inefficient Cre-mediated recombination of both *Tek* alleles in a subset of brain endothelial cells that underwent KRIT1 LOF and PI3K gain-of-function.

To test the requirement for TIE2 using a model of CCM formation conferred solely by CCM LOF, we next performed genetic rescue using the neonatal CCM model as described above for VEGFR2. A single intragastric dose of 4-OHT administered on P1 significantly reduced TIE2 expression in brain endothelial cells by P11, measured using both western blotting of brain lysate and immunostaining for TIE2$^+$; CD31$^+$ endothelial cells in hindbrain sections (Fig. 4, G–K). At P11, CD31$^+$ endothelium in the hindbrain demonstrated an ∼70% loss of TIE2 in *Cdh5-Cre*^{ERT2}; *Krit1*$^{fl/fl}$; *Tek*$^{fl/fl}$ neonates compared with controls (Fig. 4 K). Histologic, visual, and microCT assessment of lesion formation in the hindbrain at P11 demonstrated that *Tek* genetic loss effectively blocked lesion formation in neonatal brains (Fig. 4, J–N). Importantly, in contrast to loss of endothelial VEGFR2, TIE2 loss did not reduce total brain volume (Fig. 4 O), suggesting that its effects on lesion growth are unlikely to be secondary to general angiogenic-suppressive effects. Remarkably, we also found that *Tek* haploinsufficiency in brain endothelial cells was sufficient to prevent CCM lesion formation in this model (Fig. 4, M and N). This finding is similar to the observation that loss of one allele of either *Map3k3* or *Klf2* is also sufficient to almost completely prevent lesion formation (Zhou et al., 2016b), suggesting an epistatic relationship between MEKK3–KLF2/4 and TIE2. Taken together, these findings identify TIE2 as a key MEKK3–KLF2/4 effector that is required for CCM lesion formation *in vivo*.

Endothelial TIE2 expression is regulated by MEKK3–KLF2/4 signaling and acts upstream of PI3K in CCM pathogenesis

How is TIE2 signaling upregulated by loss of CCM function? Loss of CCM function and gain of MEKK3 function result in increased expression of the KLF2 and KLF4 transcription factors that prior studies have shown to be essential for CCM lesion formation in mice (Zhou et al., 2016b; Cuttano et al., 2016). Thus, a transcriptional mechanism connected to KLF2/4 function is likely to link to augmented TIE2 function during CCM formation (Pham et al., 2024). Since prior studies have demonstrated that MEKK3–KLF2/4 signaling augments PI3K signaling and a recent study suggests that PI3K gain of function alone is sufficient to increase TIE2 phosphorylation (Kraft et al., 2025), it is possible that the increase in TIE2 expression and signaling we observed was not a direct downstream effect of KLF2/4 activity and instead lay downstream of PI3K signaling. To address whether TIE2 gain-of-function lies upstream or downstream of PI3K activity, we next examined pTIE2 staining using the adult mouse craniotomy model and the Ai14 Cre reporter to detect Cre-expressing cells 7 days after AAV-Cre injection as reported above (Fig. 5, A–D). *Krit1*$^{fl/fl}$; Ai14, *iPik3ca*^{H1047R}; Ai14, and Ai14 only control animals were injected with AAV-Cre, and brains were harvested on POD 7 (Fig. 5, A and B). Immunostaining of the tdTomato-positive regions revealed elevated pTIE2 in brains with induced *Krit1* deletion alone but not in those with induced PI3K gain-of-function alone or in Ai14-only controls (Fig. 5, C and D). The latter finding is in contrast to what has recently been

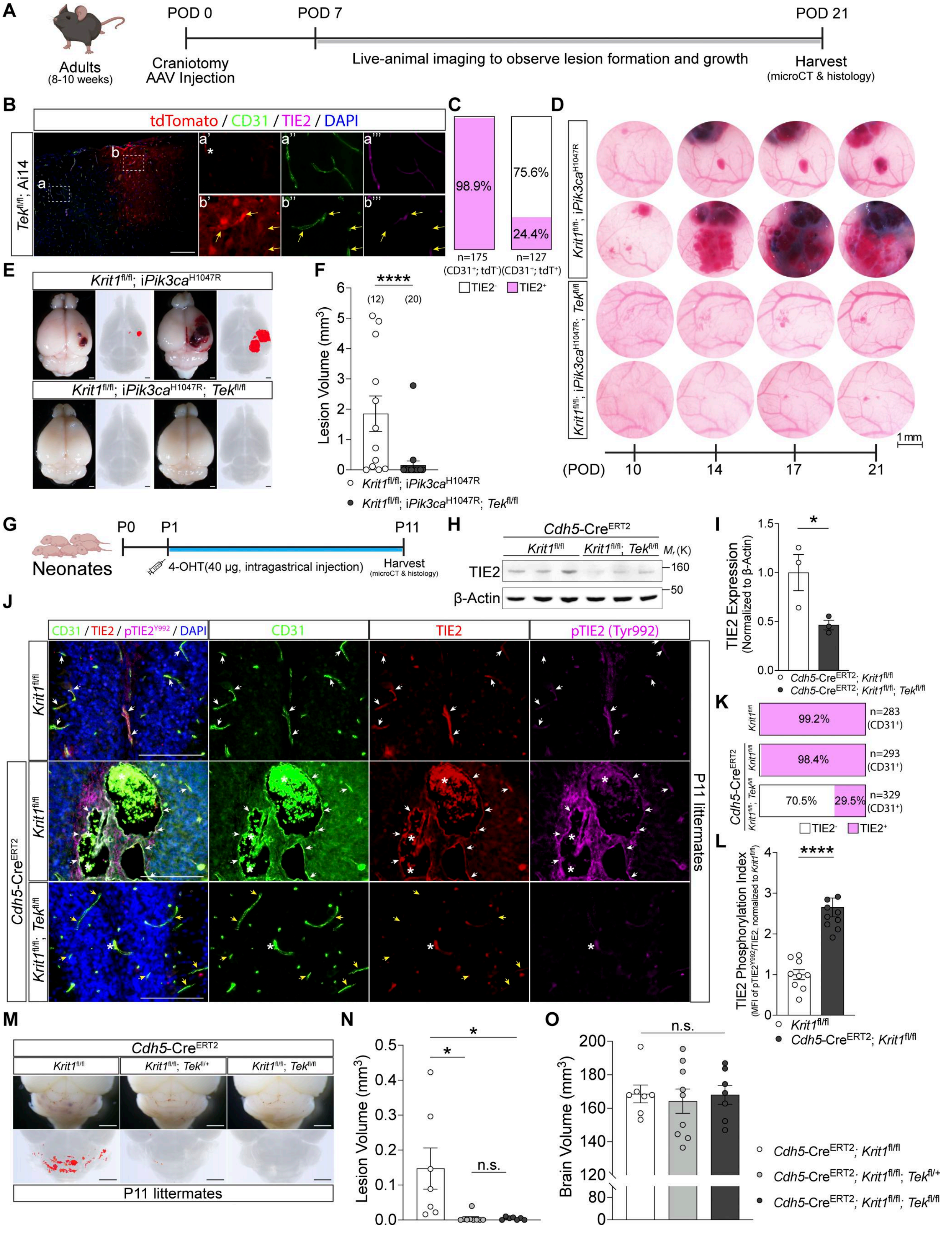

Figure 4. **Genetic deletion of TIE2 prevents CCM formation in both adult and neonatal mouse brains. (A)** Schematic representation of adult *Krit1*$^{fl/fl}$; *iPik3ca*^{H1047R} mice or *Krit1*$^{fl/fl}$; *iPik3ca*^{H1047R}; *Tek*$^{fl/fl}$ mice, aged 8–10 wk, underwent craniotomy and received focal AAV-Cre injections. Live-animal microscopic

images were captured through the cranial window from POD 7 to POD 21 to observe lesion formation and growth. **(B)** Representative images showing immunostaining for tdTomato, CD31, and TIE2, with DAPI counterstaining in brains harvested from *Tek*$^{fl/fl}$; Ai14 mice on POD 7. The boxed regions in the tdTomato-negative regions (a) and in the tdTomato-positive regions (b) are shown in a′–a′′′ and b′–b′′′, respectively, at higher magnification. Yellow arrows indicate CD31-positive but TIE2-negative endothelial cells in the tdTomato-positive regions (tdTomato$^+$, CD31$^+$, and TIE2$^-$). Scale bar: 100 µm. **(C)** Quantification of TIE2-positive (CD31$^+$; TIE2$^+$) and TIE2-negative (CD31$^+$; TIE2$^-$) endothelial cells in both tdTomato-negative and -positive regions. **(D)** Serial of microscopic images through the cranial windows showing CCM growth in either *Krit1*$^{fl/fl}$; *iPik3ca*^{H1047R} or *Krit1*$^{fl/fl}$; *iPik3ca*^{H1047R}; *Tek*$^{fl/fl}$ mouse brains from POD 10 to POD 21. **(E and F)** Representative visual images (left panels) and microCT renders (right panels), and (F) microCT quantification of CCM lesion volumes in *Krit1*$^{fl/fl}$; *iPik3ca*^{H1047R} (*n* = 12) or *Krit1*$^{fl/fl}$; *iPik3ca*^{H1047R}; *Tek*$^{fl/fl}$ (*n* = 20) mouse brains harvested on POD 21. The same microCT renders are also shown in Fig. S4 A to provide a comprehensive overview of genotype-dependent effects on lesion burden across the entire study cohort. Scale bar: 1 mm. **(G)** Schematic representation of neonatal induction of *Krit1* deletion with or without *Tek* deletion. 4-OHT was intragastrically injected on P1, and brains were harvested on P11. **(H)** Immunoblot detection of TIE2 in neonatal cerebellum harvested from P11 littermates. β-Actin was used as a loading control. **(I)** Quantification of immunoblotting for TIE2 protein level. A total of three paired littermates were measured and quantified. **(J)** Representative images showing immunostaining for CD31, TIE2, and pTIE2, with DAPI counterstaining in neonatal brains harvested from P11 littermates. White arrows indicate CD31 and TIE2 double-positive (CD31$^+$; TIE2$^+$) cells and yellow arrows indicate CD31-positive but TIE2-negative (CD31$^+$; TIE2$^-$) cells at the lesional and non-lesional neonatal cerebellum. Asterisks indicate autofluorescence emitted from lumenal red blood cells. Scale bar: 100 µm. **(K)** Quantification of TIE2-positive (CD31$^+$; TIE2$^+$) and TIE2-negative (CD31$^+$; TIE2$^-$) cerebellar endothelial cells. **(L)** Quantification of MFI of pTIE2^{Y992} in *Krit1*^{ECKO} (*Cdh5-Cre*^{ERT2}; *Krit1*$^{fl/fl}$) neonatal cerebellum, normalized to total TIE2, compared with vasculature in the normal littermate control (*Krit1*$^{fl/fl}$). **(M–O)** Representative visual images (top panels) and microCT renders (bottom panels), and microCT quantification of (N) CCM lesion volumes and (O) total brain volumes in *Cdh5-Cre*^{ERT2}; *Krit1*$^{fl/fl}$ (*n* = 7), *Cdh5-Cre*^{ERT2}; *Krit1*$^{fl/fl}$; *Tek*$^{fl/+}$ (*n* = 9), and *Cdh5-Cre*^{ERT2}; *Krit1*$^{fl/fl}$; *Tek*$^{fl/fl}$ (*n* = 7) mouse brains harvested on P11. Scale bar: 1 mm. Data shown are means ± SEM. $^*P < 0.05$ and $^{****}P < 0.0001$ by two-tailed Mann–Whitney *U* test (F and L), unpaired two-tailed *t* test (I), and one-way ANOVA, followed by Tukey HSD post hoc test (N and O). No statistically significant (n.s.) differences are observed in (N) P = 0.9997 and (O) P = 0.8649. Source data are available for this figure: SourceData F4. Tukey HSD, Tukey's honestly significant difference.

described following PI3K gain of function in dermal venous blood vessels (Kraft et al., 2025), perhaps reflecting differences between the brain and skin vasculature. These findings demonstrate that increased PI3K signaling does not strongly stimulate TIE2 expression or activity in the adult brain vasculature, consistent with a model in which gain of MEKK3–KLF2/4 signaling confers increased TIE2 expression and signaling following loss of KRIT1/CCM complex function. To further clarify the functional relationship between TIE2 and PI3K signaling in CCM pathology, we quantified phospho-S6–positive brain endothelial cells in neonatal brains following *Krit1* deletion, with or without concurrent TIE2 deletion (Fig. 5, E and F). Consistent with previous reports (Li et al., 2023; Ren et al., 2021), *Krit1* deletion caused a robust increase in the numbers of phosphorylated S6 (pS6)-positive ECs, a reliable and quantifiable marker of PI3K activity. In the control *Krit1*$^{fl/fl}$ neonatal brain with naturally highly angiogenic activity during brain development, 48% of CD31-positive cells were pS6 positive, whereas this proportion increased to ∼75% in *Cdh5-Cre*^{ERT2}; *Krit1*$^{fl/fl}$ brains. Importantly, simultaneous deletion of both KRIT1 and TIE2 in *Cdh5-Cre*^{ERT2}; *Krit1*$^{fl/fl}$; *Tek*$^{fl/fl}$ animals reduced the percentage of pS6-positive ECs to 51%, a level comparable with that in controls (Fig. 5, E and F), demonstrating that TIE2 is required for PI3K activation in the context of CCM formation.

To further address whether KLF2/4 regulate TIE2 expression, we first used CRISPR/Cas9 genome editing to delete *KRIT1* in cultured HUVECs. CRISPR/Cas9-mediated depletion of KRIT1 in HUVECs was highly efficient, with virtually no detectable KRIT1 protein in cells transduced with *KRIT1* guide RNAs compared with control guide RNAs (Fig. 5 G). Consistent with prior *in vitro* and *in vivo* studies, elimination of KRIT1 in HUVECs conferred a significant increase in KLF4 protein (Fig. 5 G). Importantly, loss of KRIT1 was also associated with a fourfold increase in TIE2 protein (Fig. 5, G and H), a change similar in magnitude to that detected for KLF4. To test whether these biochemical studies performed in cultured HUVECs are consistent with the *in vivo* findings, we isolated mouse brain endothelial cells from neonatal brains carrying *Cdh5*-Cre^{ERT2}; *Krit1*$^{fl/fl}$ alleles. Tamoxifen-induced *Krit1* deletion in these cells resulted in a ninefold increase in total TIE2 expression as well as increased KLF4 expression (Fig. 5, I and J), mirroring our *in vitro* biochemical findings in HUVECs. These studies demonstrate that loss of CCM function or gain of KLF2/4 function is sufficient to increase the expression of the TIE2 receptor in both cultured venous endothelial cells and brain vascular endothelial cells *in vivo*.

To test whether the rise in TIE2 can be directly attributed to the increase in KLF2/4 expression following *KRIT1* deletion, we transduced HUVECs with lentiviruses that express V5-tagged KLF4 in a doxycycline-inducible manner. Transient overexpression of the V5-tagged KLF4 in HUVECs increased the expression of endothelial nitric oxide synthase, a known KLF4 target gene, as well as of TIE2 (Fig. 5, K and L). Consistent with these findings, loss of *KLF2/4* or *MAP3K3*, induced by siRNAs, resulted in decreased TIE2 expression in both control and *KRIT1*-deleted HUVECs (Fig. 5, M and N).

To further determine whether TIE2 functions upstream of PI3K in CCM pathogenesis, we quantified pTIE2 (pTYR), phosphorylated AKT, and pS6 in HUVEC cultures following CRISPR/Cas9-mediated depletion of KRIT1, with or without ANGPT1 and BAY-826, a TIE2-selective agonist and inhibitor, respectively (Fig. 5 O). Consistent with our *in vivo* findings, loss of KRIT1 in HUVECs resulted in a significant increase in phosphorylation of TIE2, AKT, and S6. These phosphorylation events were effectively suppressed by the TIE2-selective inhibitor BAY-826 (Fig. 5, O and P).

Collectively, our data further support a mechanism in which increased MEKK3–KLF2/4 signaling augments PI3K signaling by increasing TIE2 expression and activity in brain endothelial cells during CCM formation (Fig. 5 M).

Pharmacologic blockade of TIE2 prevents CCM formation in adult mice

The primary therapeutic approach for symptomatic CCMs is surgical resection. However, CCMs may arise at sites in the CNS

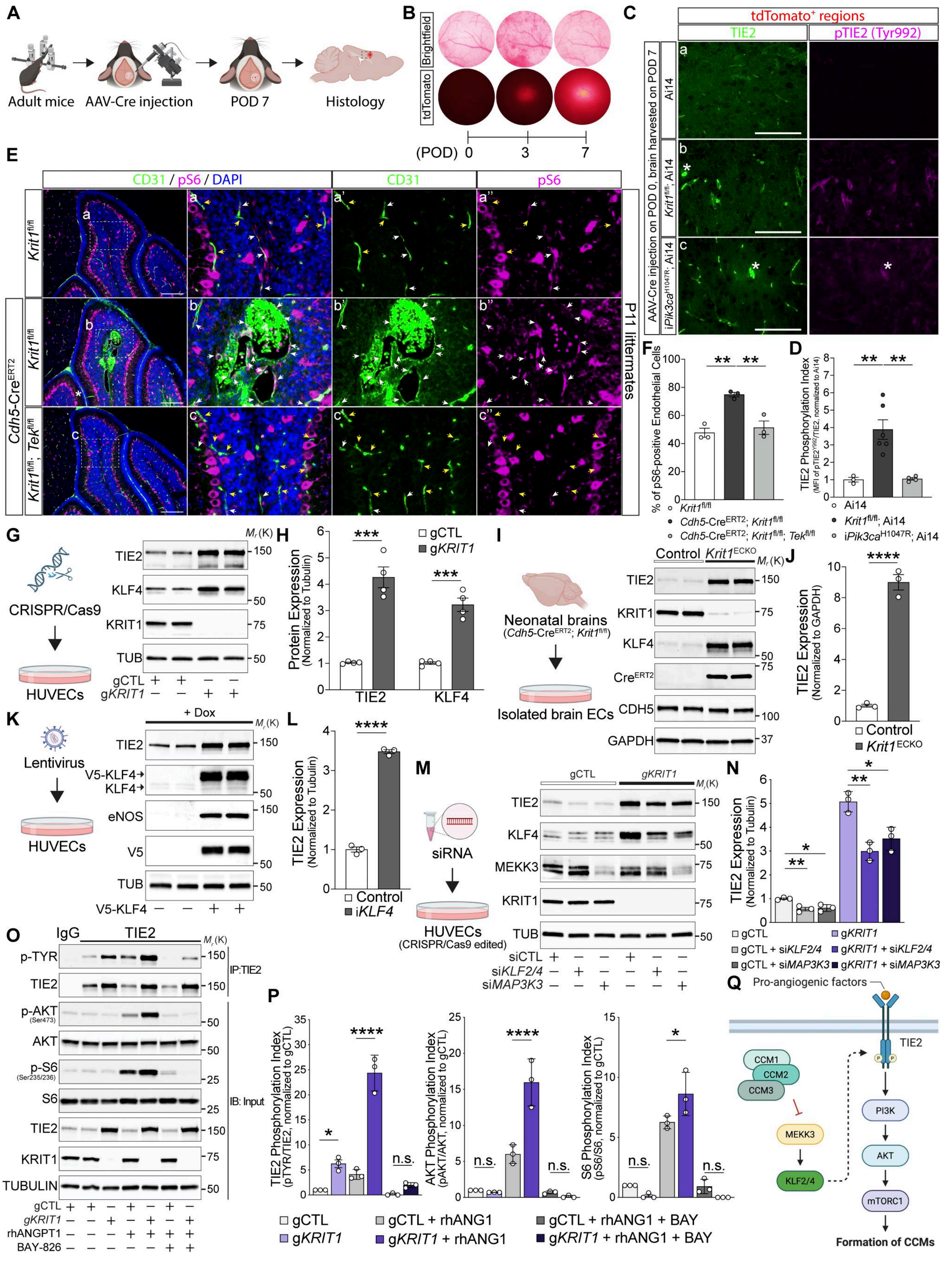

Figure 5. **Endothelial TIE2 expression and activity are increased following loss of CCM function or gain of KLF4 function, acting upstream of PI3K in CCM pathogenesis. (A)** Schematic representation of adult mice, aged 8–10 wk, undergoing craniotomy followed by focal AAV-Cre injection. Brains were

harvested on POD 7, followed by histology studies. **(B)** Representative live-animal fluorescence microscopy showing tdTomato reporter signals following focal AAV-Cre injection through the cranial window. **(C)** Representative images showing immunostaining for TIE2 and pTIE2 in adult brains harvested on POD 7 from (a) Ai14 only, (b) *Krit1*$^{fl/fl}$; Ai14, and (c) i*Pik3ca*^{H1047R}; Ai14. Asterisks indicate autofluorescence emitted from lumenal red blood cells. **(D)** Quantification of MFI of pTIE2^{Y992}, normalized to total TIE2 in the tdTomato-positive regions, as compared with the tdTomato-negative regions in the brain. A total of three to six mice in each group were measured and quantified. **(E)** Representative images showing immunostaining for CD31 and pS6, with DAPI counterstaining in neonatal brains harvested from of P11 littermates. White arrows indicate CD31 and pS6 double-positive (CD31$^+$; pS6$^+$) cells and yellow arrows indicate CD31-positive but pS6-negative (CD31$^+$; pS6$^-$) cells at the lesional and non-lesional neonatal cerebellum. **(F)** Quantification of pS6-positive (CD31$^+$; TIE2$^+$) and pS6-negative (CD31$^+$; TIE2$^-$) cerebellar endothelial cells. A total of three independent litters were measured and quantified. **(G)** Immunoblot detection of TIE2 and KLF4 in control and *KRIT1*-KO HUVECs. Cells were generated by lentiviral transduction of Cas9 with control (gCTL) or KRIT1-targeting (g*KRIT1*) gRNAs. **(H)** Quantification of immunoblotting for TIE2 and KLF4 relative to TUB protein (*n* = 4 independent experiments). **(I)** Immunoblot detection of TIE2 and KLF4 in isolated mouse brain endothelial cells carrying *Cdh5-Cre*^{ERT2}; *Krit1*$^{fl/fl}$ alleles. GAPDH was used as a loading control. **(J)** Quantification of immunoblotting for TIE2 relative to GAPDH protein (*n* = 3 independent experiments). **(K)** Immunoblot detection of TIE2 and KLF4 in HUVECs transduced with doxycycline (Dox)-inducible control and V5-KLF4–encoding lentiviruses. Cells were treated with 200 ng/ml Dox for 48 h. **(L)** Quantification of immunoblotting for TIE2 relative to TUB protein (*n* = 3 independent experiments). **(M)** Immunoblot detection of TIE2, KLF4, and MEKK3 in CRISPR/Cas9-edited HUVECs (gCTL or g*KRIT1*) following 48 h siRNA-mediated knockdown of *KLF2/4* (si*KLF2/4*), *MAP3K3* (si*MAP3K3*), or scrambled control (siCTL). **(N)** Quantification of immunoblotting for TIE2 relative to TUB protein (*n* = 3 independent experiments). **(O)** Immunoprecipitation of TIE2 from gCTL and g*KRIT1* HUVECs treated with recombinant human ANGPT1 and the TIE2 inhibitor BAY-826, followed by immunoblot analysis using the indicated antibodies. **(P)** Quantification of p-TYR, p-AKT, and p-S6 levels normalized to total TIE2, AKT, and S6, respectively (*n* = 3 independent experiments). **(Q)** Model depicting the regulation of TIE2 expression and function downstream of CCM-MEKK3–KLF2/4 signaling that links to PI3K-mTORC1 signaling to drive the formation of CCMs. Scale bar: 100 µm. Data shown are means ± SEM. *P <0.05; **P <0.01; ***P <0.001; ****P <0.0001 by two-tailed independent *t* test (H, J, and L) and one-way ANOVA, followed by Tukey HSD post hoc test (D, F, N, and P). No statistically significant (n.s.) differences are observed in P (left to right: P = 0.7395, 0.9998, 0.9946, 0.7696, and 0.7401). Source data are available for this figure: SourceData F5.

---

where surgical resection confers a high risk of neurologic deficit or is not technically feasible. Thus, medical therapies for CCM disease are desirable. However, such therapies are likely to require chronic, life-long administration and therefore must be both effective and well-tolerated. Agents that target the PI3K–mTOR pathway have been shown to block CCM disease in adult models and are used for related venous and lymphatic malformations in humans but are limited clinically by gastrointestinal, hematologic, and other side effects (Skaro et al., 2006; Lagrèze et al., 2019). Our discovery that TIE2 is required for CCM formation in both the adult mouse model for sporadic CCM and the neonatal mouse model for familial CCM suggested that targeting TIE2 signaling pharmacologically could be an attractive alternative therapy, especially as TIE2 expression is low outside of the endothelial and hematopoietic compartment. To evaluate whether TIE2 inhibition could serve as a potential therapeutic approach for CCM treatment, we investigated the efficacy of the TIE2 inhibitor rebastinib (DCC-2036) that was previously tested in a *PDCD10*-deficient neonatal mouse model (Zhou et al., 2021). Adult *Krit1*$^{fl/fl}$; i*Pik3ca*^{H1047R} mice aged 8–10 wk underwent craniotomy, followed by AAV-Cre injection. Mice were randomly assigned to two groups, receiving either rebastinib (10 mg/kg) or vehicle (a solution of 10% DMSO, 40% PEG300, 5% Tween-80, and 45% saline) by oral gavage immediately after full recovery from anesthesia. Treatment was continued every 24 h until POD 21 (Fig. 6 A). In vehicle-treated mice, CCM lesions were typically observed between POD 7 and POD 14 through the cranial window and grew rapidly thereafter as previously described (Ren et al., 2021; Li et al., 2023) (Fig. 6 B). In contrast, rebastinib-treated mice showed almost no lesion formation throughout the 21-day treatment period (Fig. 6, B–E). Notably, only 2 out of 13 mice developed detectable CCM lesions based on visual and microCT analysis (Fig. 6, B and D; and Fig. S5, A–C). These results compare favorably with our previous studies using rapamycin to inhibit mTORC1 signaling and suggest that TIE2 inhibition can effectively prevent *de novo* CCM formation even when it arises due to a two-hit mechanism involving gain of *PIK3CA* function. We recently demonstrated that rapamycin can arrest the growth of CCM lesions using the two-hit adult CCM model, an experiment that more closely mimics treatment of human patients who present with an existing, symptomatic CCM. To test whether rebastinib can also arrest the growth of existing lesions, we began treatment on POD 11 in mice with CCM lesions measuring between 0.5 and 1.0 mm in diameter based on visual assessment using the cranial window (an approach previously used to assess rapamycin [Li et al., 2023]) (Fig. 6, F and G; and Fig. S5 D). In this model rebastinib exhibited a more modest effect, including a small, nonsignificant reduction in lesion size measured using blinded micro-CT (Fig. 6, H–J), and a small, nonsignificant protection from lethality commonly associated with very large lesion formation (Fig. 6 K and Fig. S5 F). These findings are consistent with our mechanistic studies demonstrating that TIE2 gain-of-function lies downstream of MEKK3–KLF2/4 signaling but not PI3K signaling and would therefore be predicted to block part, but not all, of the pathogenic signaling driving CCM formation *in vivo*.

Discussion

In the past two decades, human genetic studies, studies using mouse and zebrafish models, and *in vitro* studies of endothelial cells have revealed a molecular pathway in which loss of CCM complex function confers gain of MEKK3 signaling and increased KLF2/4 expression, leading to the formation of vascular lesions (Fisher et al., 2015; Renz et al., 2015; Cullerea et al., 2015; Zhou et al., 2015; Cuttano et al., 2016; Boulday et al., 2011; Zhou et al., 2016b). However, defining precisely how this pathway and elevated KLF2/4 expression create vascular malformations has remained elusive. A clue to this puzzle came from recent studies demonstrating that the MEKK3–KLF2/4 pathway augments PI3K signaling in brain endothelial cells and synergizes with primary PI3K gain-of-function mutations. The present study identifies

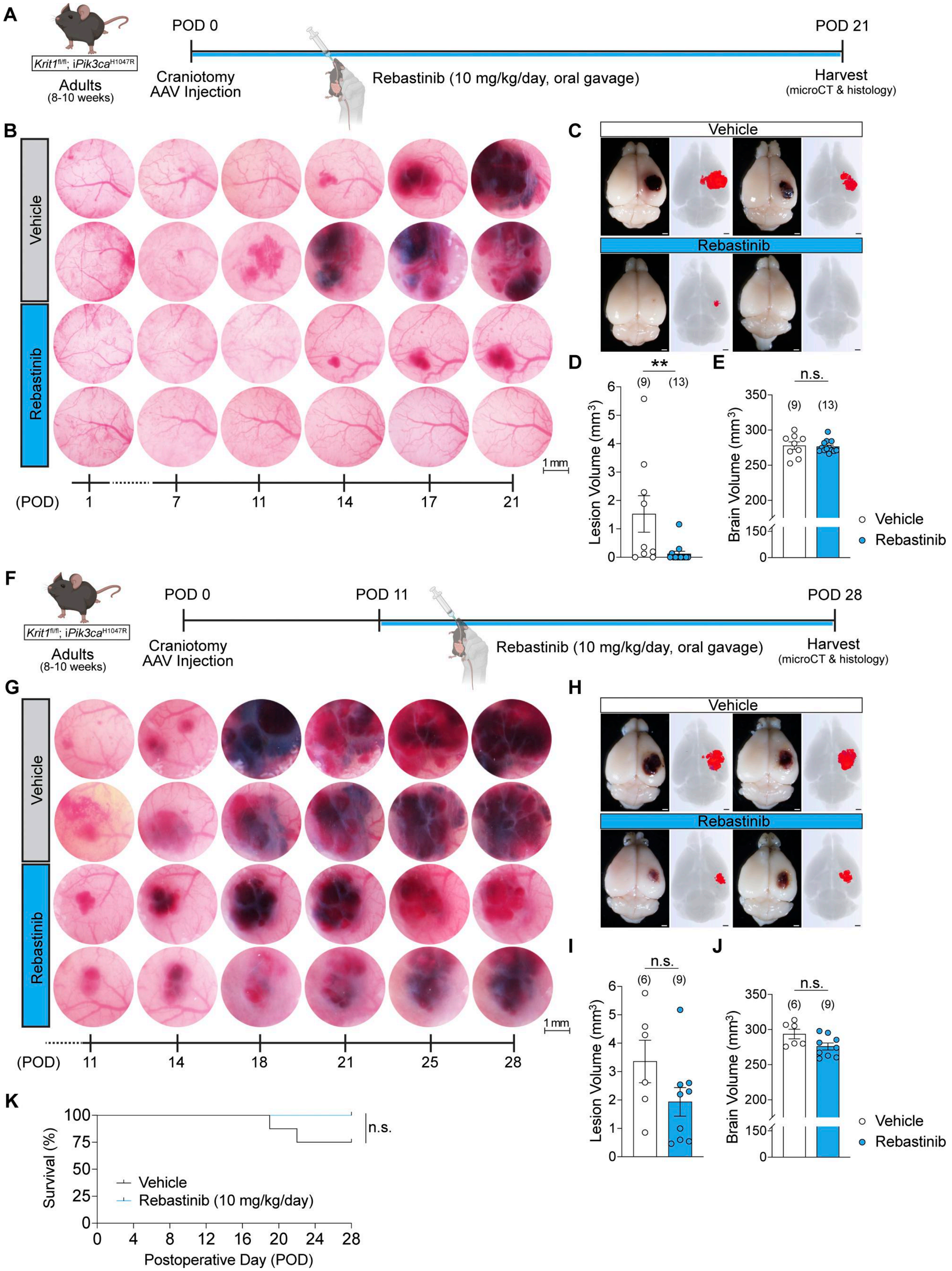

Figure 6. **Oral rebastinib treatment prevents CCM formation but does not arrest CCM growth in the two-hit adult mouse model. (A)** Schematic representation of adult *Krit1*$^{fl/fl}$; i*Pik3ca*^{H1047R} mice, aged 8–10 wk, underwent craniotomy and received focal AAV-Cre injections. Mice were randomly assigned

to receive either rebastinib (10 mg/kg) or vehicle by oral gavage immediately after full recovery from anesthesia. Treatment was continued every 24 h until POD 21. Live-animal microscopic images were captured through the cranial window from POD 7 to POD 21 to observe lesion formation and growth. **(B)** Serial of microscopic images through the cranial windows showing CCM growth in either vehicle- or rebastinib-treated mouse brains from POD 1 to POD 21. **(C–E)** Representative visual images (left panels) and microCT renders (right panels), and microCT quantification of (D) CCM lesion volumes (E) and total brain volumes of adult brains harvested on POD 21. Vehicle, *n* = 9; rebastinib, *n* = 13. The same microCT renders are also shown in Fig. S5 A to provide a comprehensive overview of the effects of rebastinib treatment on lesion burden across the entire study cohort. **(F)** Schematic representation of adult *Krit1*$^{fl/fl}$; *iPik3ca*^{H1047R} mice, aged 8–10 wk, undergoing craniotomy, followed by focal AAV-Cre injection. Mice with CCM lesion size between 0.5 and 1.0 mm on POD 11 were randomly assigned to receive either rebastinib (10 mg/kg) or vehicle by oral gavage. Treatment was continued every 24 h until POD 28. Live-animal microscopic images were captured through the cranial window from POD 11 to POD 28 to observe lesion formation and growth. **(G)** Serial of microscopic images through the cranial windows showing CCM growth in either vehicle- or rebastinib-treated mouse brains from POD 11 to POD 28. The same microscopic images are also shown in Fig. S5 F to provide a comprehensive overview of the effects of rebastinib treatment on lesion burden across the entire study cohort. **(H–J)** Representative visual images (left panels) and microCT renders (right panels), and microCT quantification of (I) CCM lesion volumes (J) and total brain volumes of adult brains harvested on POD 21. Scale bar: 1 mm. **(K)** Kaplan–Meier survival curves showing animal loss of the study. Vehicle, *n* = 8; rebastinib, *n* = 9. Data shown are means ± SEM. $^{**}P < 0.0001$ by two-tailed Mann–Whitney *U* test. No statistically significant (n.s.) differences are observed in (E) P = 0.6825, (K) P = 0.1208, (I) P = 0.1447, and (J) P = 0.0879.

TIE2 receptor expression and function as a molecular link by which augmented MEKK3–KLF2/4 signaling drives PI3K and creates venous vascular malformations. This finding extends our understanding of the molecular pathogenesis of CCM disease and identifies TIE2, a relatively endothelial-specific receptor, as a target to suppress the growth of CCM lesions that are high risk for surgical resection.

Although both VEGF receptor and TIE receptor signaling have been implicated in CCM lesion formation (DiStefano et al., 2014; He et al., 2010; DiStefano and Glading, 2020; Zhou et al., 2016a; Zhou et al., 2021), the identification of TIE2 as the molecular link between the CCM and the PI3K pathways is consistent with a body of recent studies implicating TIE2 in both developmental and pathologic venous growth and linking the receptor to PI3K signaling in venous endothelial cells. Loss of TIE2 in the developing mouse embryo confers a selective loss of venous growth (Chu et al., 2016). In contrast, gain-of-function mutations in TIE2 underlie both inherited and sporadic forms of venous malformation (Uebelhoer et al., 2013), which are also caused by gain-of-function mutations in *PIK3CA* (Limaye et al., 2015) that respond to the mTOR inhibitor rapamycin (Seront et al., 2019). These observations are consistent with the fact that CCMs arise specifically in postcapillary venules and require PI3K–mTOR signaling. Thus, it is reasonable to consider CCMs a highly aggressive and somewhat tissue specific (i.e., CNS) form of venous malformation.

A key question raised by our studies, and those of prior investigators, is the nature of the molecular mechanism by which MEKK3–KLF2/4 signaling augments TIE2-PI3K signaling during CCM formation. A prior study by Zhou et al. (2015) first implicating TIE2 signaling in CCM pathogenesis suggested that loss of CCM function might augment TIE2 signaling due to the presence of increased caveolae in CCM-deficient brain vascular ECs (Zhou et al., 2015). However, a causal relationship between changes in brain vascular EC caveolae number and TIE2 signaling was not demonstrated. More recently, Kraft et al. (2025) reported loss of the inhibitory TIE2 ligand ANGPT2 in venous ECs with PIK3CA gain of function (Kraft et al., 2025), supporting a positive feedback loop in which ANGPT1-TIE2 activation lies downstream of PI3K signaling. In contrast, our genetic studies—especially those using the neonatal model—clearly demonstrate that TIE2 signaling lies upstream, not downstream, of PI3K signaling during CCM formation. Our present studies suggest that one mechanism by which CCM deficiency and augmented KLF2/4 activity increases TIE2-PI3K signaling is through upregulation of TIE2 receptor expression. However, this observation does not explain how those TIE2 receptors are activated to generate PI3K signaling and why that activation, and therefore the disease, is so specific for the CNS. Prior studies by our group identified the upregulation of genes encoding ADAMTS proteases that cleave versican as a causal downstream mechanism for both CCM formation in the postnatal brain (Hong et al., 2020) and cardiac defects in the developing embryo (Zhou et al., 2015) following loss of CCM function. Significantly, both the developing heart and postnatal brain are sites of high versican matrix. How might these observations be connected to the role of TIE2? The angiopoietins that activate TIE2 are expressed by neighboring cells, e.g., pericytes for ANGPT1, or by endothelial cells, e.g., ANGPT2, to control vascular stability versus remodeling and growth. It is possible that ADAMTS expression at sites of high perivascular versican such as the CNS releases matrix-bound angiopoietin ligands that are then able to act on upregulated TIE2 receptors to drive PI3K signaling. Future studies addressing the nature and source of TIE2 ligands during CCM formation will be required to test this model.

A potential translational implication of this study is the possibility of targeting the TIE2 receptor to prevent and/or arrest CCM growth. Our previous studies demonstrated that the mTOR antagonist rapamycin can prevent and arrest CCM growth conferred either by loss of CCM function alone in the neonatal model or by combined loss of CCM function and gain of *PIK3CA* function in the adult model that more closely reproduces sporadic human CCM lesions. While these studies are promising and consistent with recent use of PI3K and mTOR inhibitors to treat related venous and lymphatic malformations (Skaro et al., 2006; Lagrèze et al., 2019; Boscolo et al., 2015; Hammer et al., 2018; Maruani et al., 2021; Wiegand et al., 2022; Seront et al., 2023; Adams et al., 2016; Wenger et al., 2022; Zerbib et al., 2024; Luu et al., 2024), the PI3K pathway is broadly utilized *in vivo*, and its inhibition is associated with significant cutaneous, hematologic, and gastrointestinal side effects that limit the use and tolerance of such therapeutics. In contrast, TIE2 receptor expression and function are much more restricted, impacting primarily vascular endothelial and hematopoietic cells. The recent emergence of therapies to block TIE2 or its angiopoietin ligands reviewed by Saharinen et al. (2017), and the efficacy of rebastinib in the adult mouse CCM model suggest that these agents might provide a means of treating CCM disease medically with fewer off-target effects. However, in the two-hit adult CCM mouse model that reproduces the genetic pathology underlying most symptomatic CCM lesions (Li et al., 2023; Ren et al., 2021), rebastinib appears less effective at arresting existing lesion growth than rapamycin. The basis for this difference is suggested by our mechanistic studies: while both gain of MEKK3–KLF2/4 signaling and gain of *PIK3CA* function confer increased PI3K–mTOR signaling, TIE2 appears to be a specific MEKK3–KLF2/4 effector. Thus, blockade of TIE2 is predicted to block input from selectively this pathway and not from the *PIK3CA* gain-of-function mutation. In contrast, agents that directly target PI3K or mTOR are predicted to block input from both pathogenic mutations and provide a more complete reversal of pathogenic signaling. It is conceivable, however, that combining effective TIE2 blockade with a lower level of PI3K or mTOR inhibition could generate an effective and better tolerated approach to medical treatment of surgically unresectable CCMs. Finally, it is worth noting that the angiopoietin ligands and the TIE2 receptor likely function primarily on the abluminal surface of the brain endothelium and thus lie on the other side of the blood–brain barrier. Whether agents such as blocking antibodies could reach their targets and effectively block TIE2 signaling remains to be determined.

Limitations of the present study

Although we believe that the adult cranial window approach closely models human sporadic CCM, Cre activity in this model stimulates expression of *PIK3CA* H1047R from the *Rosa26* locus rather than the endogenous locus. This results in both a quantitative and qualitative increase in *PIK3CA* activity that likely exceeds the gain-of-function in human lesions. The pharmacologic agents used in our study show relative specificity for TIE2 and VEGFR2, but these agents have activity at multiple tyrosine kinase domains. We have addressed this technical limitation with genetic LOF strategies for both receptors. Finally, it is possible that TdT expression from the highly sensitive Ai14 reporter overestimates the true deletion efficiency at the *Kdr* locus. However, this possibility does not alter our functional conclusions because the combined loss of *Krit1* and *Kdr* produced a significantly greater number of CCM lesions than loss of *Krit1* alone, a phenotype that precludes a pathogenic role for VEGFR2 and that would be underestimated rather than overestimated if Ai14 reporter expression exceeded true VEGFR2 deletion efficiency.

Materials and methods

Collection of human brain tissues

Human CCM tissue specimens were freshly obtained from surgical resections performed at the Hospital of the University of Pennsylvania, Philadelphia, PA, USA, following approval by the institution's Institutional Review Board (protocol no. 845196; IRB). Surgical decisions were made independently by the treating physicians, based on clinical indications unrelated to this study. The diagnosis of CCM was confirmed through pathological assessment.

Non-CCM control brain tissue specimens were obtained from the Hospital of the University of Pennsylvania, Philadelphia, PA, USA, and the University of Chicago, Chicago, IL, USA (protocol no. 859512 and 10-295-A, respectively), following approval by the respective IRBs. Tissue collection was performed either during neurosurgical procedures or through postmortem donation, with all decisions made independently by the treating physicians and families based on clinical circumstances unrelated to this study.

Patient informed consent

Human samples were obtained with informed consent from all donors. All samples were de-identified prior to analysis, and the study was approved by the IRB.

Mice

Cdh5-Cre$^{\mathrm{ERT2}}$ (Wang et al., 2010), *Krit1*$^{\mathrm{fl/fl}}$ (Chan et al., 2011), R26-LSL-*Pik3ca*$^{\mathrm{H1047R}}$ (*iPik3ca*$^{\mathrm{H1047R}}$) (Adams et al., 2011), and *Tek*$^{\mathrm{fl/fl}}$ (Qu et al., 2019) have been described previously. *Kdr*$^{\mathrm{fl/fl}}$ (JAX, # 018977) (Hooper et al., 2009) and R26-LSL-RFP (Ai14, #007914; JAX) (Madisen et al., 2010) were obtained from the Jackson Laboratories.

For all adult mouse CCM experiments, *Krit1*$^{\mathrm{fl/fl}}$; R26-LSL-*Pik3ca*$^{\mathrm{H1047R}}$ (*Krit1*$^{\mathrm{fl/fl}}$; *iPik3ca*$^{\mathrm{H1047R}}$) transgenic mice, with or without additional alleles such as *Kdr*$^{\mathrm{fl/fl}}$, *Tek*$^{\mathrm{fl/fl}}$, and Ai14, were bred and housed in a pathogen-free vivarium approved by the Association for Assessment and Accreditation of Laboratory Animal Care at the University of Pennsylvania, Philadelphia, PA, USA. Both male and female mice, aged 8–10 wk, were used in all experiments.

For all neonatal mouse CCM experiments, *Cdh5*-Cre$^{\mathrm{ERT2}}$; *Krit1*$^{\mathrm{fl/fl}}$ transgenic mice, with or without additional alleles such as *Kdr*$^{\mathrm{fl/fl}}$ and *Tek*$^{\mathrm{fl/fl}}$, were bred and housed in a pathogen-free environment as described above. On P1, pups were intragastrically injected with 40 μg of 4-OHT (#H7904; MilliporeSigma) dissolved in 9% ethanol/corn oil vehicle (total volume 50 μl per injection) using a 30-gauge needle. The solution was freshly prepared from premeasured, 4-OHT powder for each injection. The P1 time point was determined by checking experimental breeding pairs every evening for new litters. The following morning (P1), pups were injected with 4-OHT in a blinded fashion without knowledge of genotypes. Littermate controls were used in all neonatal experiments unless otherwise specified.

All mice were housed in individually ventilated cages on a 12:12-h light-dark cycle, with food and water provided ad libitum. All animal protocols and experiments were approved by the Institutional Animal Care and Use Committee at the University of Pennsylvania, Philadelphia, PA, USA, and conducted in accordance with relevant guidelines and regulations. Preclinical studies adhered to the updated ARRIVE 2.0 guidelines.

Sex as a biological variable

Our study examined male and female animals, and similar findings are reported for both sexes.

Craniotomy surgery

Animals were anaesthetized with isoflurane (3.0% induction, 1.0–2.0% maintenance in 1.0 liters/min oxygen) for surgery. Mice were placed on a heating pad covered with a cotton pad to maintain a body temperature of 37.5°C. The depth of anesthesia was periodically monitored by testing the animal's reflexes through toe pinch. Ophthalmic lubricant was applied to the eyes to prevent dryness. A stereotactic frame (Stoelting Instruments) was used to immobilize the head with ear bars. Mice undergoing craniotomies received 1.5 mg/kg of dexamethasone intramuscularly (Sigma-Aldrich) and 5 mg/kg of 10% meloxicam (Midwest Vet Supply) subcutaneously. After immobilization, the scalp hair was removed with Nair, and the scalp was cleaned and sterilized with betadine, followed by 70% ethanol, repeated at least three times. The scalp was then removed to expose the skull. The periosteum was carefully removed with blunt forceps. The outer table of the skull was thinned using a handheld high-speed dental drill (Foredom) using a 0.5-mm burr. For adult mice, a 4-mm diameter circular craniotomy was performed over the right somatosensory cortex posterior to the coronal suture. Sterile saline was used to irrigate the drill burr, preventing bone residue buildup and drill overheating. Gelfoam in sterile saline was applied for hemostasis and to remove bone dust. The border of the craniotomy was thinned until the inner table fractures. The craniotomy border was thinned until the inner table fractured. A fine-tip forceps (Fine Science Tools) or up-angled curette (Fine Science Tools) was used to lift the bone flap and gently separate it from the dura. Gelfoam was used to maintain hemostasis and prevent the brain surface from desiccating.

Following the completion of intraparenchymal viral injection, hemostasis was obtained. A cranial window, made from a 5-mm glass coverslip (Warner), was placed over the craniotomy site and secured to the skull using cyanoacrylate glue and dental cement (Keystone). Immediately following surgery, mice were monitored closely and kept separately from their littermates until they were awake and mobile.

AAV injection

Recombinant AAV(BR1)-CAG-Cre (AAV-Cre) was purchased from SignaGen Laboratories (#SL116069). Immediately following craniotomy, recombinant AAV vectors carrying Cre recombinase under the control of the CAG promoter were injected into the right somatosensory cortex centered on +1.5 mm lateral and −1.0 mm posterior to bregma at a depth of 0.5 mm using a beveled glass micropipette. A total of 1×10^9 viral genomes in 100 nl sterile PBS were gradually injected over 5 min for each mouse to enhance viral diffusion and minimize damage to brain tissue.

Oral rebastinib administration

Rebastinib was purchased from MedChemExpress (#HY-13024). Mice were randomly assigned into two groups and received either rebastinib (10 mg/kg) or vehicle (a solution of 10% DMSO, 40% PEG300, 5% Tween-80, and 45% saline by volume) via oral gavage. Treatment was administered daily within a 2-h window.

microCT and volumetric quantification

For all experiments utilizing microCT quantification of CCM lesion volume, brains were harvested and stored in 4% (wt/vol) PFA/PBS (pH 7.4). The brains were kept in fixative until staining with nondestructive iodine contrast, followed by microCT imaging, as previously described (Girard et al., 2016). Tissue processing, imaging, and volume quantification were performed in a blinded manner by investigators at the University of Chicago, Chicago, IL, USA, with no knowledge of genotype or experimental details.

Histology, immunohistochemistry, and quantification

Human CCM tissue specimens were freshly obtained from surgical resection at the Hospital of the University of Pennsylvania, Philadelphia, PA, USA. Tissues were stored in ice-cold PBS and processed for histology within 1 h after surgery. Mice were euthanatized with CO_2 asphyxiation, followed by transcardial perfusion with 20 ml of cold PBS, followed by 4% PFA/PBS (pH 7.4). Both human and mouse tissues were harvested and fixed in 4% PFA/PBS overnight, dehydrated in 100% ethanol, and embedded in paraffin. Tissue sections (6 μm thickness) underwent dewaxing and rehydration through xylene and ethanol and were subsequently used for H&E, Prussian blue, and immunohistochemistry staining. Antibodies used are listed in Table S1. Control and experimental tissue sections were stained simultaneously under identical conditions. Sections were mounted on slides with ProLong Gold Antifade reagent. Images were acquired using Olympus BX53 microscope equipped with 4, 10, 20, and 40× objectives and subsequently processed in cellSens (Olympus) and ImageJ software (National Institutes of Health; NIH).

Quantification of median fluorescent intensities (MFIs) was performed using ImageJ software (NIH). In brains with no visible lesions, MFI in the region of interest (ROI) was determined by the immunostaining of tdTomato reporter in the brain region that received focal AAV-Cre injection following craniectomy. TdTomato-positive regions were contoured, and MFI for TIE2, pTIE2, VEGFR2, and pVEGFR2 were measured using the contoured ROI in their corresponding fluorescent channels. Identical contoured ROI was applied to the contralateral side of the brain section to obtain background fluorescent intensities for background subtraction. In brains with CCM lesions, MFI in the ROI was determined by the immunostaining of CD31-positive lesional endothelium. The protein phosphorylation index was calculated as the MFI of phosphorylated protein (e.g., pTIE2) over total protein (e.g., TIE2). The ratio was used to compare different experimental groups. A total of three sections, spaced 120 μm apart, from each of the mouse brain (three to six individual animals per group) were analyzed and quantified.

Cell culture

Pooled HUVECs were purchased from Lonza (#CC-2519) and cultured in endothelial basal medium (EBM, Lonza) supplemented with hydrocortisone (1 μg/ml), bovine brain extract (12 μg/ml), gentamicin (50 μg/ml), human recombinant epidermal growth factor (10 ng/ml), and 10% FBS (Life Technologies). Human embryonic kidney cells (HEK293FT) were purchased from Life Technologies (#R70007) and cultured in DMEM supplemented with 10% FBS (Life Technologies) and gentamicin (50 μg/ml, Lonza). Cells were tested negative for mycoplasma and maintained at 37°C in a humidified atmosphere with 5% CO_2.

Lentivirus generation and transductions

For doxycycline-inducible lentiviral expression of a human V5-tagged KLF4 (isoform 1), cDNA was cloned into pLVX–Te-tOne–Puro (Clontech) and co-transfected into HEK293FT with lentiviral packaging vectors pMD2.G (no. 12259; Addgene) and psPAX2 (no. 12260; Addgene) using Lipofectamine 2000 (Life Technologies), and viruses were harvested after 24 and 48 h. HUVECs were infected with viruses for 24 h in the presence of 8 µg/ml polybrene (#SC-134220; Santa Cruz Biotechnology) and selected with 1 µg/ml puromycin (#ant-pr-1; InvivoGen). KLF4 expression was induced with 200 ng ml^{-1} doxycycline (no. D9891; Sigma-Aldrich) for 48 h.

CRISPR/Cas9 genome editing of HUVECs

KRIT1-specific gRNA sequences (Table S2) were cloned into the plentiCRISPRv2 plasmid (#52961; Addgene) and co-transfected with the packaging vectors for lentivirus production as described above. Scramble guide RNA sequences were used as a control.

RNA interference

Control (gCTL) or KRIT1-KO (gKRIT1) HUVECs were transfected with 50 nM of ON-TARGETplus SMARTpool siRNAs (Dharmacon) listed in Table S2 using Lipofectamine RNAiMAX (Invitrogen) according to the manufacturer's recommendations. Cell lysates were taken 48 h after transfection for western blot.

rhANGPT1 and BAY-826 treatment of HUVECs

To induce TIE2 phosphorylation in HUVEC cultures, recombinant human ANGPT1 (rhANGPT1; #923-AN-025/CF; R&D Systems) was reconstituted in PBS and applied to HUVECs at 200 ng/ml for 30 min. To inhibit TIE2 phosphorylation, cells were pre-treated with the TIE2 kinase inhibitor BAY-826 (1 µM; #6579; Tocris) for 20 min prior to rhANGPT1 stimulation.

Isolation of brain endothelial cells and *ex vivo* culture

Brains from P11 *Cdh5*-Cre$^{\mathrm{ERT2}}$; *Krit1*$^{\mathrm{fl/fl}}$ mice injected with 4-OHT (P1–P3) were minced and enzymatically digested with 0.5% collagenase type II (#C6885; Sigma-Aldrich) in DMEM (#42430; Gibco) at 37°C for 10 min under stirring (300 rpm). The resulting cell suspension was filtered through a 40-mm nylon strainer (BD falcon), centrifuged at 300 g for 10 min, and the pellet was resuspended in DMEM supplemented with 10% FBS. Cells were incubated at RT for 45 min with VECAD (#555289; BD Pharmingen) and ICAM2 (#553326; BD Pharmingen) antibody-conjugated Dynabeads (#11035; Invitrogen) previously. Microvascular fragments were magnetically separated and resuspended in DMEM/F12 (Invitrogen) supplemented with 15% FCS, endothelial growth factor (#C-30140; PromoCell), and penicillin and streptomycin. Cells were plated on collagen-coated (#C5533; Sigma-Aldrich) culture dishes. Upon confluence, ECs were repurified using PECAM1 antibody (#553370; BD Pharmingen) and seeded for downstream assays. No additional passaging was performed.

Immunoprecipitation and protein immunoblotting

Immunoprecipitation and analysis of TIE2 phosphorylation were performed as previously described (Jo et al. 2021). Control (gCTL) and KRIT1-knockout (gKRIT1) HUVECs were serum starved for 6 h in EBM medium (Lonza) supplemented with 0.1% (vol/vol) BSA (#1595; Sigma-Aldrich) prior to the indicated treatments. Cells were lysed in IP buffer (10 mM Tris-HCl, pH 7.4; 150 mM NaCl; 5 mM EDTA; 10% glycerol; 1% Triton X-100) freshly supplemented with 1X protease/phosphatase inhibitor cocktail (#5872; Cell Signaling Technology) and 1 mM phenylmethylsulfonyl fluoride (PMSF). Cell lysates were cleared by centrifugation at 13,000 rpm for 15 min at 4°C, and protein concentrations were quantified using the Bradford assay. Equal amounts of total protein were incubated overnight at 4°C with 1 µg anti-TIE2 antibody (#AF313; R&D Systems), followed by immunoprecipitation with 6 µl magnetic Protein G Dynabeads (#10-003-D; Invitrogen) for 2 h. Beads were washed three times with IP buffer, and bound proteins were eluted at 95°C for 10 min in 4X SDS sample buffer before immunoblot analysis.

Western blot analyses were performed with precast gradient gels (Thermo Fisher Scientific) using standard methods. Briefly, brain tissues or HUVECs were homogenized in RIPA buffer (R26200-125.0; Research Products International) supplemented with cOmplete protease inhibitor cocktail (#11697498001; Roche) and PhosSTOP phosphatase inhibitor cocktail (#4906845001; Roche). For brain lysates, proteins were separated by a NuPAGE 4–12% Bis-Tris Mini Protein Gel (#NP0335BOX; Thermo Fisher Scientific) with NuPAGE MOPS SDS Running Buffer (#NP0001; Thermo Fisher Scientific) and transferred onto Immobilon-FL PVDF membrane (#IPFL00010; Millipore) using Mini Trans-Blot Cell (Bio-Rad). For HUVEC lysates, proteins were resolved by SDS-PAGE using Criterion TGX Precast gels (Bio-Rad) and transferred onto nitrocellulose membranes using the Trans Turbo Blot system (Bio-Rad). Membranes were blocked in 5% BSA or 5% milk + 0.01% Tween-20 in TBS 1× for 1 h at room temperature. Primary antibodies in blocking buffer were incubated overnight at 4°C. Peroxidase- or fluorophore-conjugated secondary antibodies were incubated for 1 h at room temperature. Chemiluminescent protein detection was visualized using Clarity Western ECL kit (Bio-Rad) and the ChemiDoc MP Imaging System (Bio-Rad) and quantified using Image Lab software (Bio-Rad). Fluorescence protein detection was performed on the LI-COR Odyssey FC system and quantified and normalized to β-actin using ImageStudio software. Antibodies used are listed in Table S1.

Statistics

No statistical methods were used to predetermine sample size. All experimental and control animals were littermates, and none was excluded from analyses at the time of harvest. Data were analyzed using GraphPad Prism software and are presented as means ± SEM. P values were calculated using two-tailed independent *t* test, unpaired Welch's *t* test, Mann–Whitney *U* test, Mantel–Cox test, or ANOVA followed by Tukey's honestly significant difference post hoc test for multiple comparisons, as indicated in the figure legends. P values of < 0.05 were considered statistically significant and are denoted as follows: $^{*}P < 0.05$, $^{**}P < 0.01$, $^{***}P < 0.001$, and $^{****}P < 0.0001$.

Online supplemental material

Supplemental material includes extended experimental data that could not be fully presented in the main figures, additional control experiments, and supporting figures that further validate the findings in the main text. Tables S1 and S2 list all antibodies and gRNA and siRNA sequences used in this study. Figures S1, S2, S3, S4, and S5 provide additional controls validating cranial window surgery and AAV focal delivery, extended immunohistochemistry analyses, microCT rendered images with lesion quantification of mouse brains, and additional phenotypic validations.

Data availability

All data supporting the findings of this study are available within the main text or the supplementary materials. Additional raw data, materials, and protocols are available from the corresponding author upon reasonable request.

Acknowledgments

We thank the University of Chicago, Chicago, IL, USA, PaleoCT core facility for its expertise in imaging and image quantification.

This work was supported by National Institutes of Health (NIH) grant R01HL094326 (M.L. Kahn), NIH grant R01NS100949 (M.L. Kahn), NIH grant P01NS092521 (M.L. Kahn, I.A. Awad, and D.A. Marchuk), Leducq Foundation (M.L. Kahn), AHA Postdoctoral Fellowship 906488 (S. Gao), Adelman CCM fund (J.-K.Burkhardt), Deutsche Forschungsgemeinschaft, SFB 1531 – 456687919 (M. Potente), and DZHK (German Center for Cardiovascular Research), partner site Berlin (M. Potente).

Author contributions: Lun Li: conceptualization, data curation, formal analysis, investigation, methodology, project administration, resources, supervision, validation, visualization, and writing—original draft, review, and editing. Marco Castro: data curation, formal analysis, investigation, methodology, validation, visualization, and writing—review and editing. Hiroki Hongo: data curation, investigation, visualization, and writing—review and editing. Jian Ren: data curation and investigation. Robert Shenkar: investigation and writing—review and editing. Rashad Jabarkheel: conceptualization, data curation, investigation, methodology, and writing—review and editing. Siqi Gao: investigation. Sweta Narayan: investigation. Maxwell Frankfurter: conceptualization and writing—review and editing. Alan T. Tang: conceptualization, investigation, and methodology. Jisheng Yang: investigation. Mei Chen: conceptualization and investigation. Jenna Bockman: formal analysis and investigation. Patricia Mericko-Ishizuka: project administration and resources. Roberto Alcazar: formal analysis, investigation, and writing—review and editing. Georgio Sader: investigation and methodology. Javed Iqbal: investigation, resources, software, visualization, and writing—original draft. Serena Kinkade: data curation and investigation. Rhonda Lightle: investigation. Andrew K. Ressler: investigation and writing—review and editing. Xianghu Qu: methodology, resources, and writing—review and editing. H. Scott Baldwin: resources and writing—review and editing. Douglas A. Marchuk: conceptualization, funding acquisition, supervision, and writing—review and editing. Issam A. Awad: formal analysis, funding acquisition, methodology, validation, visualization, and writing—review and editing. Jan-Karl Burkhardt: conceptualization, formal analysis, methodology, project administration, supervision, and writing—review and editing. Michael Potente: funding acquisition, methodology, supervision, and writing—review and editing. Mark L. Kahn: conceptualization, formal analysis, funding acquisition, methodology, project administration, resources, supervision, and writing—original draft, review, and editing.

Disclosures: I.A. Awad reported personal fees from Neurelis and from Ovid Rx outside the submitted work. No other disclosures were reported.

Submitted: 7 July 2025
Revised: 26 November 2025
Accepted: 10 February 2026

References

Adams, D.M., C.C. Trenor, A.M. Hammill, A.A. Vinks, M.N. Patel, G. Chaudry, M.S. Wentzel, P.S. Mobberley, L.M. Campbell, C. Brookbank, et al. 2016. Efficacy and safety of sirolimus in the treatment of complicated vascular anomalies. *Pediatrics*. 137:e20153257. https://doi.org/10.1542/PEDS.2015-3257

Adams, J.R., K. Xu, J.C. Liu, N.M. Ruiz Agamez, A.J. Loch, R.G. Wong, W. Wang, K.L. Wright, T.F. Lane, E. Zacksenhaus, and S.E. Egan. 2011. Cooperation between Pik3ca and p53 mutations in mouse mammary tumor formation. *Cancer Res.* 71:2706–2717. https://doi.org/10.1158/0008-5472.CAN-10-0738

Boscolo, E., N. Limaye, L. Huang, K.-T. Kang, J. Soblet, M. Uebelhoer, A. Mendola, M. Natynki, E. Seront, S. Dupont, et al. 2015. Rapamycin improves TIE2-mutated venous malformation in murine model and human subjects. *J. Clin. Invest.* 125:3491–3504. https://doi.org/10.1172/JCI76004

Boulday, G., N. Rudini, L. Maddaluno, A. Blécon, M. Arnould, A. Gaudric, F. Chapon, R.H. Adams, E. Dejana, and E. Tournier-Lasserve. 2011. Developmental timing of CCM2 loss influences cerebral cavernous malformations in mice. *J. Exp. Med.* 208:1835–1847. https://doi.org/10.1084/JEM.20110571

Chan, A.C., S.G. Drakos, O.E. Ruiz, A.C.H. Smith, C.C. Gibson, J. Ling, S.F. Passi, A.N. Stratman, A. Sacharidou, M.P. Revelo, et al. 2011. Mutations in 2 distinct genetic pathways result in cerebral cavernous malformations in mice. *J. Clin. Invest.* 121:1871–1881. https://doi.org/10.1172/JCI44393

Chu, M., T. Li, B. Shen, X. Cao, H. Zhong, L. Zhang, F. Zhou, W. Ma, H. Jiang, P. Xie, et al. 2016. Angiopoietin receptor Tie2 is required for vein specification and maintenance via regulating COUP-TFII. *Elife*. 5:e21032. https://doi.org/10.7554/ELIFE.21032

Cullerea, X., E. Plovieb, P.M. Bennetta, C.A. MacRaeb, and T.N. Mayadasa. 2015. The cerebral cavernous malformation proteins CCM2L and CCM2 prevent the activation of the MAP kinase MEKK3. *Proc. Natl. Acad. Sci. USA*. 112:14284–14289. https://doi.org/10.1073/PNAS.1510495112

Cuttano, R., N. Rudini, L. Bravi, M. Corada, C. Giampietro, E. Papa, M.F. Morini, L. Maddaluno, N. Baeyens, R.H. Adams, et al. 2016. KLF4 is a key determinant in the development and progression of cerebral cavernous malformations. *EMBO Mol. Med.* 8:6–24. https://doi.org/10.15252/EMMM.201505433

DiStefano, P.V., and A.J. Glading. 2020. VEGF signalling enhances lesion burden in KRIT1 deficient mice. *J. Cell Mol. Med.* 24:632–639. https://doi.org/10.1111/JCMM.14773

DiStefano, P.V., J.M. Kuebel, I.H. Sarelius, and A.J. Glading. 2014. KRIT1 protein depletion modifies endothelial cell behavior via increased vascular endothelial growth factor (VEGF) Signaling. *J. Biol. Chem.* 289: 33054–33065. https://doi.org/10.1074/jbc.M114.582304

Fisher, O.S., H. Deng, D. Liu, Y. Zhang, R. Wei, Y. Deng, F. Zhang, A. Louvi, B.E. Turk, T.J. Boggon, and B. Su. 2015. Structure and vascular function of MEKK3-cerebral cavernous malformations 2 complex. *Nat. Commun.* 6:7937. https://doi.org/10.1038/NCOMMS8937

Girard, R., H.A. Zeineddine, C. Orsbon, H. Tan, T. Moore, N. Hobson, R. Shenkar, R. Lightle, C. Shi, M.D. Fam, et al. 2016. Micro-computed tomography in murine models of cerebral cavernous malformations as a paradigm for brain disease. *J. Neurosci. Methods*. 271:14–24. https://doi.org/10.1016/J.JNEUMETH.2016.06.021

Hammer, J., E. Seront, S. Duez, S. Dupont, A. Van Damme, S. Schmitz, C. Hoyoux, C. Chopinet, P. Clapuyt, F. Hammer, et al. 2018. Sirolimus is efficacious in treatment for extensive and/or complex slow-flow vascular malformations: A monocentric prospective phase II study. *Orphanet J. Rare Dis.* 13:191. https://doi.org/10.1186/S13023-018-0934-Z

He, Y., H. Zhang, L. Yu, M. Gunel, T.J. Boggon, H. Chen, and W. Min. 2010. Stabilization of VEGFR2 signaling by cerebral cavernous malformation 3 is critical for vascular development. *Sci. Signal.* 3:ra26. https://doi.org/10.1126/SCISIGNAL.2000722

Hong, C.C., A.T. Tang, M.R. Detter, J.P. Choi, R. Wang, X. Yang, A.A. Guerrero, C.F. Wittig, N. Hobson, R. Girard, et al. 2020. Cerebral cavernous malformations are driven by ADAMTS5 proteolysis of versican. *J. Exp. Med.* 217:e20200140. https://doi.org/10.1084/JEM.20200140

Hong, T., X. Xiao, J. Ren, B. Cui, Y. Zong, J. Zou, Z. Kou, N. Jiang, G. Meng, G. Zeng, et al. 2021. Somatic MAP3K3 and PIK3CA mutations in sporadic cerebral and spinal cord cavernous malformations. *Brain*. 144: 2648–2658. https://doi.org/10.1093/BRAIN/AWAB117

Hooper, A.T., J.M. Butler, D.J. Nolan, A. Kranz, K. Iida, M. Kobayashi, H.G. Kopp, K. Shido, I. Petit, K. Yanger, et al. 2009. Engraftment and reconstitution of hematopoiesis is dependent on VEGFR2-mediated regeneration of sinusoidal endothelial cells. *Cell Stem Cell*. 4:263–274. https://doi.org/10.1016/j.stem.2009.01.006

Jo, G., J. Bae, H. Jeong Hong, A.-r. Han, D.-K. Kim, S. Pyo Hong, J.A. Kim, S. Lee, G. Young Koh, and H. Min Kim. 2021. Structural insights into the clustering and activation of Tie2 receptor mediated by Tie2 agonistic antibody. *Nat. Commun* 12:6287. https://doi.org/10.1038/s41467-021-26620-1

Kraft, M., H. Schoofs, M. Petkova, J. Andrade, A.R. Grosso, R. Benedito, A.K. De Roo, L.M. Boon, M. Vikkula, F.G. Kapp, et al. 2025. Angiopoietin-TIE$_2$ feedforward circuit promotes PIK3CA-driven venous malformations. *Nat. Cardiovasc. Res.* 4:801–820. https://doi.org/10.1038/S44161-025-00655-9

Lagrèze, W.A., L. Joachimsen, N. Gross, C. Taschner, and J. Rössler. 2019. Sirolimus-induced regression of a large orbital lymphangioma. *Orbit*. 38:79–80. https://doi.org/10.1080/01676830.2018.1436569

Lai, C.C., B. Nelsen, E. Frias-Anaya, H. Gallego-Gutierrez, M. Orecchioni, V. Herrera, E. Ortiz, H. Sun, O.A. Mesarwi, K. Ley, et al. 2022. Neuroinflammation plays a critical role in cerebral cavernous malformation disease. *Circ. Res.* 131:909–925. https://doi.org/10.1161/CIRCRESAHA.122.321129

Lee, E., E.A. Lee, E. Kong, H. Chon, M. Llaiqui-Condori, C.H. Park, B.Y. Park, N.R. Kang, J.S. Yoo, H.S. Lee, et al. 2023. An agonistic anti-Tie2 antibody suppresses the normal-to-tumor vascular transition in the glioblastoma invasion zone. *Exp. Mol. Med.* 2023 55:470–484. https://doi.org/10.1038/s12276-023-00939-9

Li, L., A.A. Ren, S. Gao, Y.S. Su, J. Yang, J. Bockman, P. Mericko-Ishizuka, J. Griffin, R. Shenkar, R. Alcazar, et al. 2023. mTORC1 inhibitor Rapamycin inhibits growth of cerebral cavernous malformation in adult mice. *Stroke*. 54:2906–2917. https://doi.org/10.1161/STROKEAHA.123.044108

Limaye, N., J. Kangas, A. Mendola, C. Godfraind, M.J. Schlögel, R. Helaers, L. Eklund, L.M. Boon, and M. Vikkula. 2015. Somatic activating PIK3CA mutations cause venous malformation. *Am. J. Hum. Genet.* 97:914–921. https://doi.org/10.1016/j.ajhg.2015.11.011

Luu, M., P. Vabres, A. Espitalier, A. Maurer, A. Garde, C. Racine, M. Carpentier, A. Rega, R. Loffroy, N. Hadouiri, et al. 2024. A phase II double-blind multicentre, placebo-controlled trial to assess the efficacy and safety of alpelisib (BYL719) in paediatric and adult patients with Megalencephaly-CApillary malformation Polymicrogyria syndrome (MCAP): The SESAM study protocol. *BMJ Open*. 14:e084614. https://doi.org/10.1136/BMJOPEN-2024-084614

Madisen, L., T.A. Zwingman, S.M. Sunkin, S.W. Oh, H.A. Zariwala, H. Gu, L.L. Ng, R.D. Palmiter, M.J. Hawrylycz, A.R. Jones, et al. 2010. A robust and high-throughput Cre reporting and characterization system for the whole mouse brain. *Nat. Neurosci.* 13:133–140. https://doi.org/10.1038/NN.2467

Maruani, A., E. Tavernier, O. Boccara, J. Mazereeuw-Hautier, S. Leducq, D. Bessis, L. Guibaud, P. Vabres, V. Carmignac, S. Mallet, et al. 2021. Sirolimus (Rapamycin) for slow-flow malformations in children: The observational-phase randomized clinical PERFORMUS trial. *JAMA Dermatol.* 157: 1289–1298. https://doi.org/10.1001/JAMADERMATOL.2021.3459

Peyre, M., D. Miyagishima, F. Bielle, F. Chapon, M. Sierant, Q. Venot, J. Lerond, P. Marijon, S. Abi-Jaoude, T. Le Van, et al. 2021. Somatic PIK3CA mutations in sporadic cerebral cavernous malformations. *N. Engl. J. Med.* 385:996–1004. https://doi.org/10.1056/NEJMOA2100440/SUPPL_FILE/NEJMOA2100440_DISCLOSURES.PDF

Pham, V.-C., C.J. Rödel, M. Valentino, M. Malinverno, A. Paolini, J. Münch, C. Pasquier, F.C. Onyeogaziri, B. Lazovic, R. Girard, et al. 2024. Epigenetic regulation by polycomb repressive complex 1 promotes cerebral cavernous malformations. *EMBO Mol. Med.* 16:2827–2855. https://doi.org/10.1038/S44321-024-00152-9

Qu, X., C. Harmelink, and H. Scott Baldwin. 2019. Tie2 regulates endocardial sprouting and myocardial trabeculation. *JCI Insight*. 4:e96002. https://doi.org/10.1172/JCI.INSIGHT.96002

Ren, A.A., D.A. Snellings, Y.S. Su, C.C. Hong, M. Castro, A.T. Tang, M.R. Detter, N. Hobson, R. Girard, S. Romanos, et al. 2021. PIK3CA and CCM mutations fuel cavernomas through a cancer-like mechanism. *Nature*. 594:271–276. https://doi.org/10.1038/s41586-021-03562-8

Renz, M., C. Otten, E. Faurobert, F. Rudolph, Y. Zhu, G. Boulday, J. Duchene, M. Mickoleit, A.C. Dietrich, C. Ramspacher, et al. 2015. Regulation of β1 integrin-Klf2-mediated angiogenesis by CCM proteins. *Dev. Cell*. 32: 181–190. https://doi.org/10.1016/j.devcel.2014.12.016

Saharinen, P., L. Eklund, and K. Alitalo. 2017. Therapeutic targeting of the angiopoietin-TIE pathway. *Nat. Rev. Drug Discov.* 16:635–661. https://doi.org/10.1038/NRD.2016.278

Seront, E., A. Van Damme, L.M. Boon, and M. Vikkula. 2019. Rapamycin and treatment of venous malformations. *Curr. Opin. Hematol.* 26:185–192. https://doi.org/10.1097/MOH.0000000000000498

Seront, E., A. Van Damme, C. Legrand, A. Bisdorff-Bresson, P. Orcel, T. Funck-Brentano, M.-A. Sevestre, A. Dompmartin, I. Quere, P. Brouillard, et al. 2023. Preliminary results of the European multicentric phase III trial regarding sirolimus in slow-flow vascular malformations. *JCI Insight*. 8: e173095. https://doi.org/10.1172/JCI.INSIGHT.173095

Shi, C., R. Shenkar, H. Du, E. Duckworth, H. Raja, H.H. Batjer, and I.A. Awad. 2009. Immune response in human cerebral cavernous malformations. *Stroke*. 40:1659–1665. https://doi.org/10.1161/STROKEAHA.108.538769

Skaro, A.I., P.J. Marotta, and V.C. McAlister. 2006. Regression of cutaneous and gastrointestinal telangiectasia with sirolimus and aspirin in a patient with hereditary hemorrhagic telangiectasia. *Ann. Intern. Med.* 144: 226–227. https://doi.org/10.7326/0003-4819-144-3-200602070-00030

Uebelhoer, M., M. Nätynki, J. Kangas, A. Mendola, H.L. Nguyen, J. Soblet, C. Godfraind, L.M. Boon, L. Eklund, N. Limaye, and M. Vikkula. 2013. Venous malformation-causative TIE2 mutations mediate an AKT-dependent decrease in PDGFB. *Hum. Mol. Genet.* 22:3438–3448. https://doi.org/10.1093/HMG/DDT198

Wang, Y., M. Nakayama, M.E. Pitulescu, T.S. Schmidt, M.L. Bochenek, A. Sakakibara, S. Adams, A. Davy, U. Deutsch, U. Lüthi, et al. 2010. Ephrin-B2 controls VEGF-induced angiogenesis and lymphangiogenesis. *Nature*. 465:483–486. https://doi.org/10.1038/NATURE09002

Wenger, T.L., S. Ganti, C. Bull, E. Lutsky, J.T. Bennett, K. Zenner, D.M. Jensen, V. Dmyterko, E. Mercan, G.M. Shivaram, et al. 2022. Alpelisib for the treatment of PIK3CA-related head and neck lymphatic malformations and overgrowth. *Genet. Med.* 24:2318–2328. https://doi.org/10.1016/j.gim.2022.07.026

Wiegand, S., A. Dietz, and G. Wichmann. 2022. Efficacy of sirolimus in children with lymphatic malformations of the head and neck. *Eur. Arch. Otorhinolaryngol.* 279:3801–3810. https://doi.org/10.1007/S00405-022-07378-8

Zerbib, L., S. Ladraa, A. Fraissenon, C. Bayard, M. Firpion, Q. Venot, S. Protic, C. Hoguin, A. Thomas, S. Fraitag, et al. 2024. Targeted therapy for capillary-venous malformations. *Signal Transduct. Target. Ther.* 9:146. https://doi.org/10.1038/S41392-024-01862-9

Zhou, H.J., L. Qin, Q. Jiang, K.N. Murray, H. Zhang, B. Li, Q. Lin, M. Graham, X. Liu, J. Grutzendler, and W. Min. 2021. Caveolae-mediated Tie2 signaling contributes to CCM pathogenesis in a brain endothelial cell-specific Pdcd10-deficient mouse model. *Nat. Commun.* 12:504. https://doi.org/10.1038/S41467-020-20774-0

Zhou, H.J., L. Qin, H. Zhang, W. Tang, W. Ji, Y. He, X. Liang, Z. Wang, Q. Yuan, A. Vortmeyer, et al. 2016a. Endothelial exocytosis of angiopoietin-2 resulting from CCM3 deficiency contributes to cerebral cavernous malformation. *Nat. Med.* 22:1033–1042. https://doi.org/10.1038/NM.4169

Zhou, Z., D.R. Rawnsley, L.M. Goddard, W. Pan, X.-J. Cao, Z. Jakus, H. Zheng, J. Yang, J.S.C. Arthur, K.J. Whitehead, et al. 2015. The cerebral cavernous malformation pathway controls cardiac development via regulation of endocardial MEKK3 signaling and KLF expression. *Dev. Cell*. 32:168–180. https://doi.org/10.1016/j.devcel.2014.12.009

Zhou, Z., A.T. Tang, W.Y. Wong, S. Bamezai, L.M. Goddard, R. Shenkar, S. Zhou, J. Yang, A.C. Wright, M. Foley, et al. 2016b. Cerebral cavernous malformations arise from endothelial gain of MEKK3-KLF2/4 signalling. *Nature*. 532:122–126. https://doi.org/10.1038/NATURE17178

Supplemental material

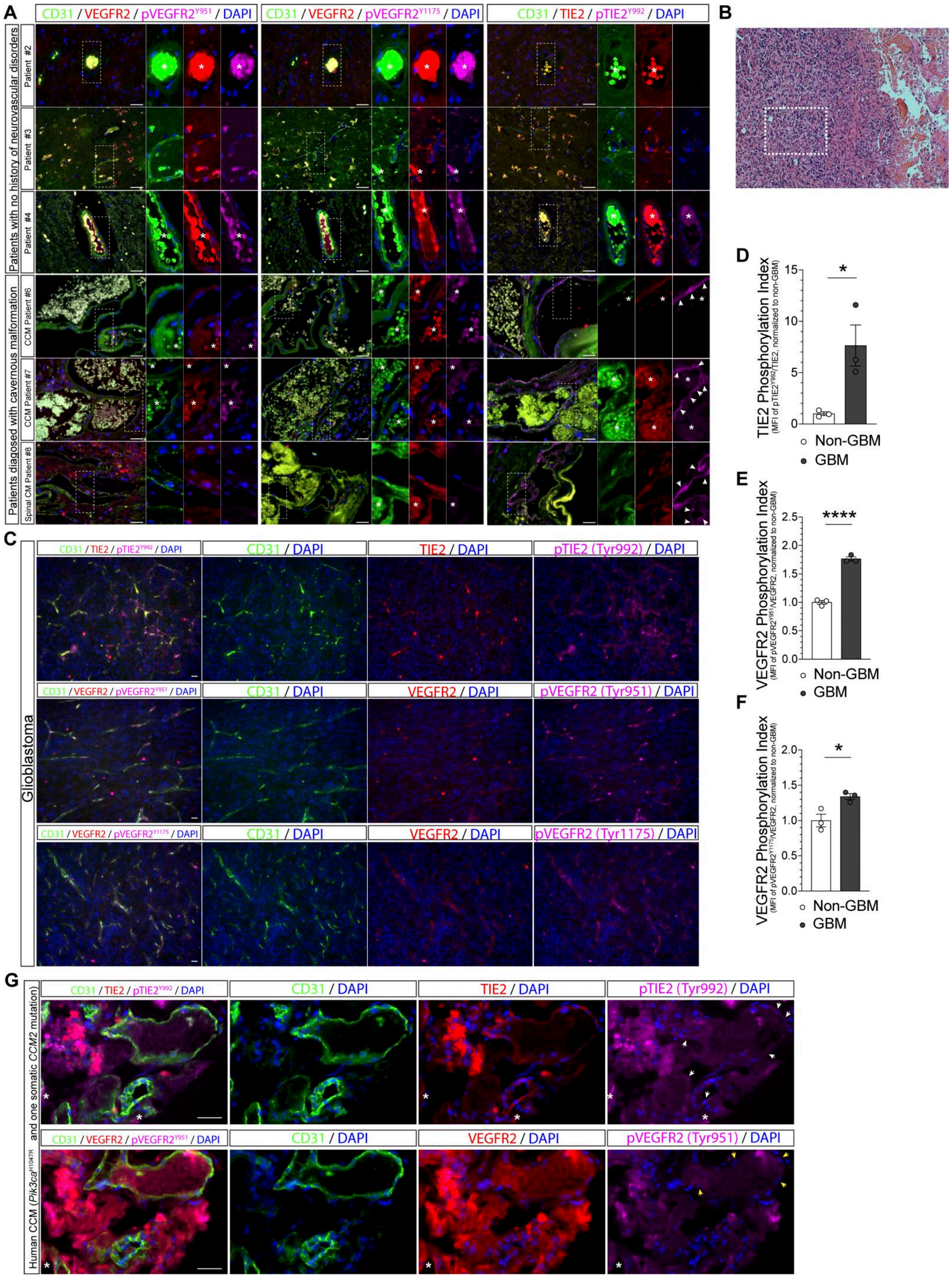

Figure S1. **Detection of pTIE2 and pVEGFR2 in human brain tissue specimens. (A)** Representative images showing immunostaining for CD31, VEGFR2, pVEGFR2, and TIE2, pTIE2, with DAPI counterstaining in freshly resected human CCM specimens and non-CCM human brain tissue. The boxed regions in the lower-magnification images are shown at higher magnification on the right. Arrows indicate pTIE2-positive endothelial cells lining CCM lesions. **(B)** Representative image of H&E staining revealing the classic histopathological appearance of glioblastoma (GBM), characterized by high cellularity and areas of necrosis. The boxed region represents high cellularity area adjacent to the necrotic tissue and is used for pVEGFR2 and pTIE2 antibodies validation and quantification in the following panels. **(C)** Representative images showing immunostaining for CD31, VEGFR2, pVEGFR2, TIE2, pTIE2, with DAPI counterstaining in resected human GBM specimen. **(D–F)** Quantification of MFI of (D) pTIE2^{Y992}, (E) pVEGFR2^{Y951}, and (F) pVEGFR2^{Y1175}, normalized to total TIE2 and VEGFR2, respectively, as compared with endothelium in non-GBM brain tissue. *N* = 3 human samples in each group were analyzed and quantified. Data shown are means ± SEM. *P <0.05, ****P <0.0001 by unpaired two-tailed Welch *t* test. **(G)** Representative images showing immunostaining for CD31, VEGFR2, pVEGFR2, TIE2, and pTIE2, with DAPI counterstaining in recovered human CCM specimen with identified lesional endothelial cell genotypes (PIK3CA^{H1047R} and somatic CCM2 mutation), as previously characterized by Ren et al. (2021). CCM sample was rederived from frozen tissue, sectioned, and processed with methanol fixation, which differs from the processing of all other tissue images (standard histology protocol described in the Materials and methods) reported in this manuscript. White arrows indicate pTIE2-positive endothelial cells lining CCM lesions. Yellow arrows indicate CD31^{-} and VEGFR2-double positive but pVEGFR2-negative endothelial cells lining CCM lesions. Asterisks denote (A) autofluorescence emitted from lumenal red blood cells and (G) tissue border autofluorescence without reliable CD31 or DAPI nuclear staining to identify endothelial cells. Scale bar: 100 μm.

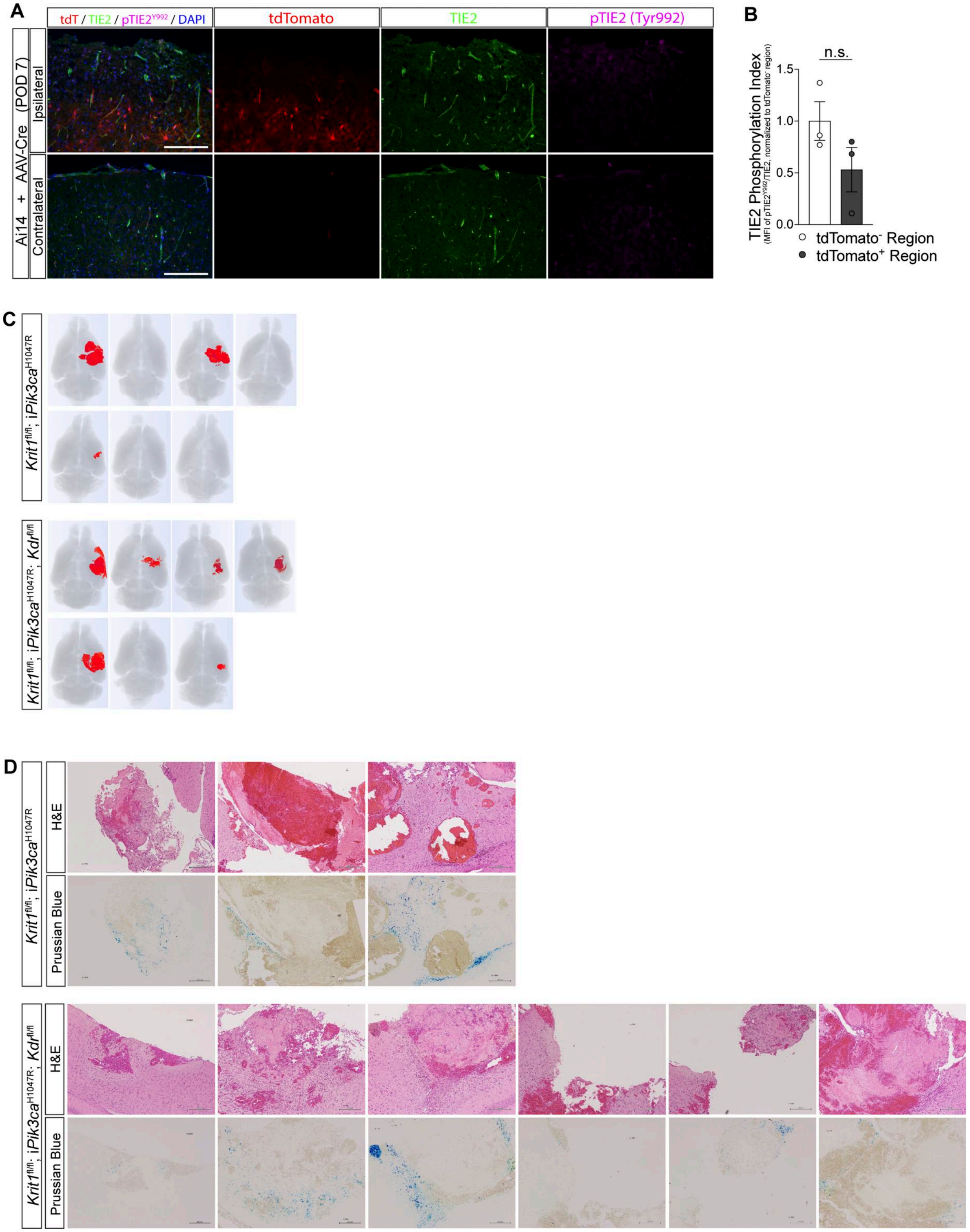

Figure S2. **TIE2 phosphorylation is unaffected by craniotomy, stereotactic injection, and AAV transduction, while VEGFR2 deletion fails to prevent CCM formation in the adult mouse model. (A)** Ai14 mice between age 8–10 wk underwent craniotomy and received AAV-Cre injections to induce focal Cre-mediated tdTomato reporter expression in the cerebral cortex below a cranial window. Representative images showing immunostaining for CD31, TIE2, and pTIE2, with DAPI counterstaining in brains harvested on POD 7. **(B)** Quantification of MFI of pTIE2^{Y992} normalized to total TIE2, compared with tdTomato-negative contralateral brain regions that received no procedure or AAV-Cre administration. A total of three mice in each group were measured and quantified. Data shown are means ± SEM. No statistically significant (n.s.) differences are observed ($P = 0.1730$) by unpaired two-tailed Welch *t* test. Scale bar: 100 µm. **(C)** MicroCT renders of all study subjects, including seven *Krit1*$^{fl/fl}$; i*Pik3ca*^{H1047R} and seven *Krit1*$^{fl/fl}$; i*Pik3ca*^{H1047R}; *Kdr*$^{fl/fl}$ mouse brains, harvested on POD 21. Two pairs of representative microCT renders from this complete cohort are presented in Fig. 3 E with the corresponding brain specimens to demonstrate genotype-dependent differences in lesion burden. **(D)** Representative images showing H&E and Prussian blue staining of *Krit1*$^{fl/fl}$; i*Pik3ca*^{H1047R} and *Krit1*$^{fl/fl}$; i*Pik3ca*^{H1047R}; *Kdr*$^{fl/fl}$ mouse brains harvested on POD 21.

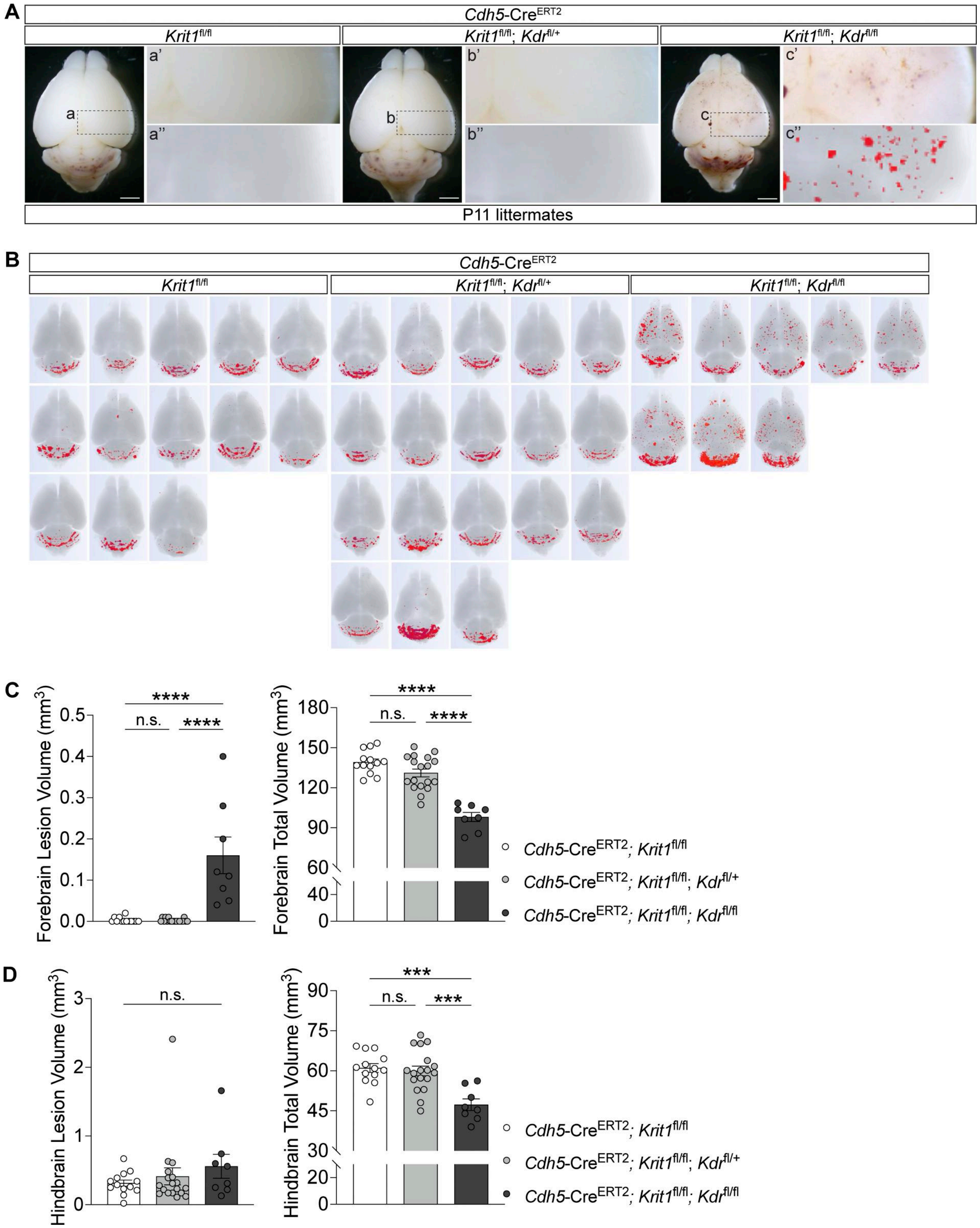

Figure S3. **Genetic deletion of VEGFR2 does not prevent CCM formation but promotes new lesion development in the forebrain in the neonatal mouse model. (A)** Representative visual images and microCT renders of *Cdh5-Cre*^{ERT2}; *Krit1*$^{fl/fl}$; *Cdh5-Cre*^{ERT2}; *Krit1*$^{fl/fl}$; *Kdr*$^{fl/+}$, and *Cdh5-Cre*^{ERT2}; *Krit1*$^{fl/fl}$; *Kdr*$^{fl/fl}$ mouse brains harvested on P11. Boxed regions of the right cerebrum (a–c) are shown in (a'–c') with pair microCT renders (a''–c''), respectively, at higher magnification. **(B)** MicroCT renders of all study subjects, *Cdh5-Cre*^{ERT2}; *Krit1*$^{fl/fl}$; *Cdh5-Cre*^{ERT2}; *Krit1*$^{fl/fl}$; *Kdr*$^{fl/+}$, and *Cdh5-Cre*^{ERT2}; *Krit1*$^{fl/fl}$; *Kdr*$^{fl/fl}$ mouse brains harvested on P11. The same brain specimens and corresponding microCT renders are shown in Fig. 3 M with emphasis on cerebellar lesions. Representative images in this panel highlight whole-brain and forebrain views. **(C and D)** microCT quantification of (C) neonatal forebrain and (D) neonatal hindbrain in *Cdh5-Cre*^{ERT2}; *Krit1*$^{fl/fl}$ (n = 13), *Cdh5-Cre*^{ERT2}; *Krit1*$^{fl/fl}$; *Kdr*$^{fl/+}$ (n = 18), and *Cdh5-Cre*^{ERT2}; *Krit1*$^{fl/fl}$; *Kdr*$^{fl/fl}$ (n = 8) mouse brains harvested on P11. Scale bar: 1 mm. Data shown are means ± SEM. ***P <0.001 and ****P <0.0001 by one-way ANOVA, followed by Tukey HSD post hoc test. No statistically significant (n.s.) differences are observed in (C) left: P = 0.9990; right: P = 0.1183 and (D) left: P = 0.4559; right: P = 0.9027. Tukey HSD, Tukey's honestly significant difference.

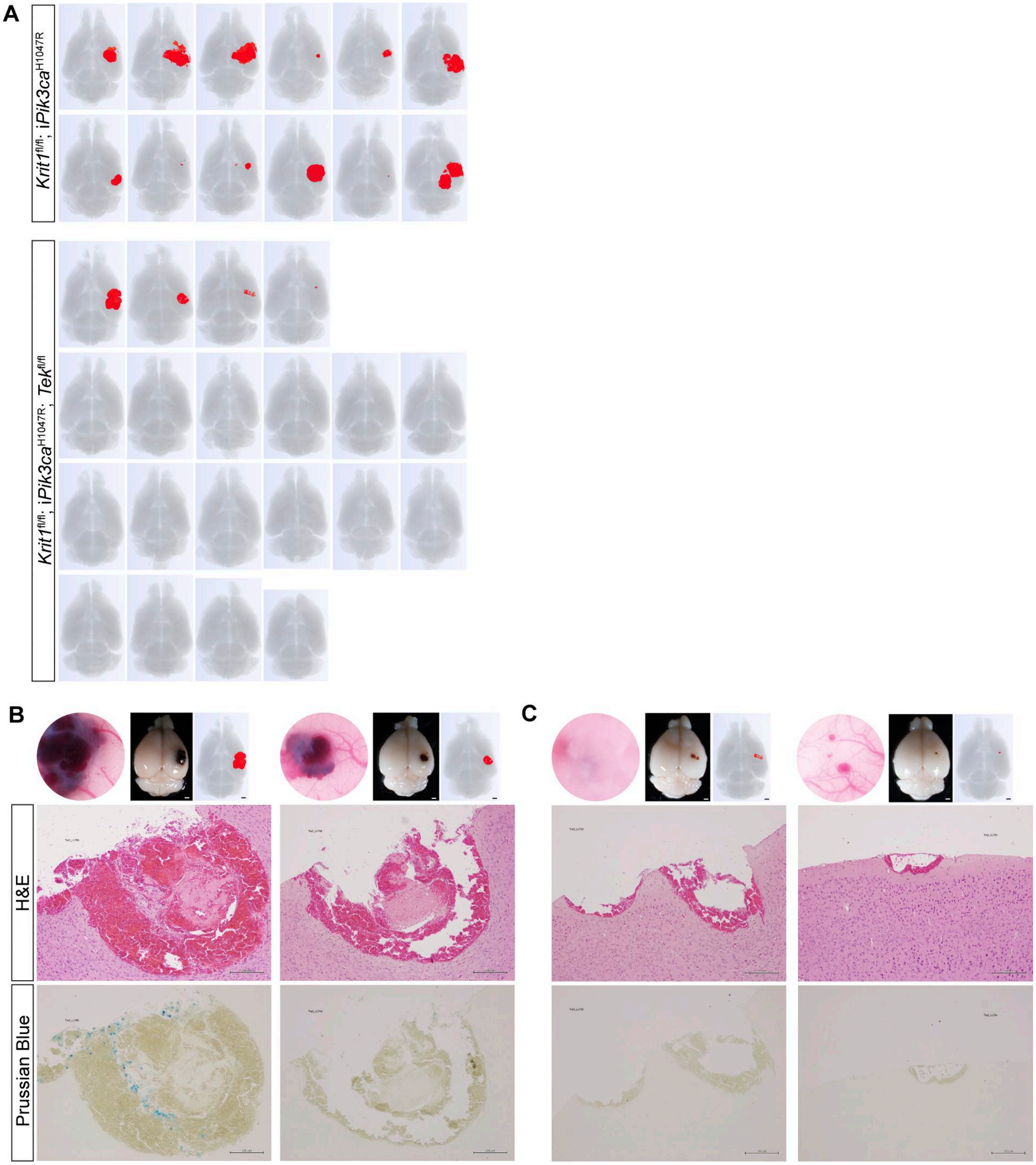

Figure S4. **Genetic deletion of TIE2 prevents CCM formation. (A)** microCT renders of all study subjects, including 12 *Krit1*$^{fl/fl}$; *iPik3ca*^{H1047R} and 12 *Krit1*$^{fl/fl}$; *iPik3ca*^{H1047R}; *Tek*$^{fl/fl}$ mouse brains, harvested on POD 21. Two pairs of representative microCT renders from this complete cohort are presented in Fig. 4 E with the corresponding brain specimens to demonstrate genotype-dependent differences in lesion burden. **(B)** Representative microscopic images through the cranial windows (top left panels), visual images (top center panels), and microCT renders (top right panels), paired with H&E and Prussian blue staining (bottom panels) from two *Krit1*$^{fl/fl}$; *iPik3ca*^{H1047R}; *Tek*$^{fl/fl}$ mice showing significant CCM lesions on POD 21. **(C)** Representative microscopic images through the cranial windows (top left panels), visual images (top center panels), and microCT renders (top right panels), paired with H&E and Prussian blue staining (bottom panels) from two *Krit1*$^{fl/fl}$; *iPik3ca*^{H1047R}; *Tek*$^{fl/fl}$ mice showing no typical CCM pathology on POD 21. Scale bar: 1 mm.

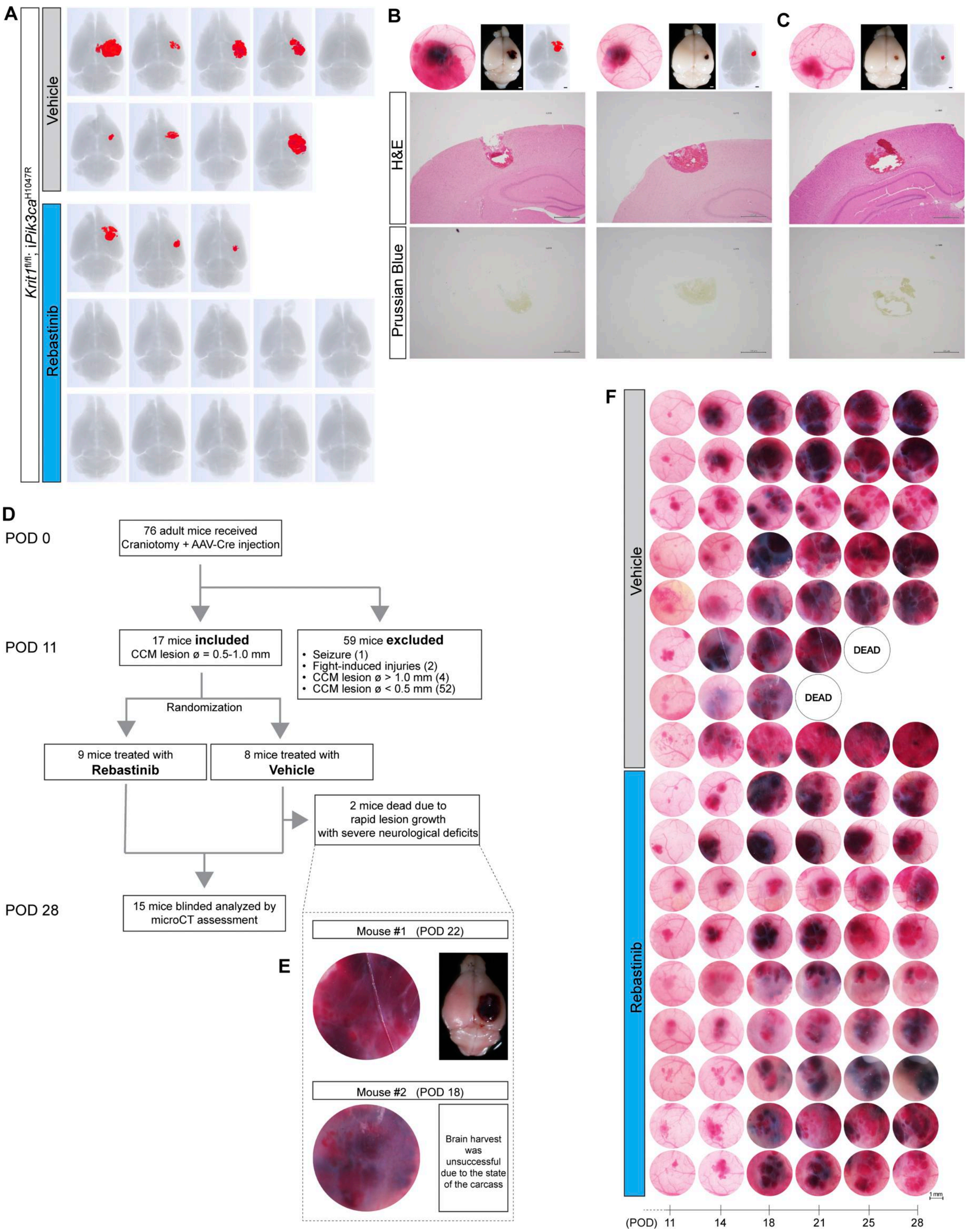

Figure S5. **Oral rebastinib treatment prevents *de novo* CCM formation but does not arrest the progression of existing lesions in the adult mice. (A)** microCT images of all study subjects, including 9 *Krit1*$^{fl/fl}$; i*Pik3ca*^{H1047R} mice treated with vehicle and 13 *Krit1*$^{fl/fl}$; i*Pik3ca*^{H1047R} mice treated with rebastinib. Mouse brains were harvested on POD 21. Two pairs of representative microCT renders from this complete cohort are presented in Fig. 6 C with the corresponding brain specimens to demonstrate the effects of rebastinib treatment in lesion burden. **(B and C)** Representative microscopic images through the cranial windows (top left panels), visual images (top center panels), and microCT renders (top right panels), paired with H&E and Prussian blue staining (bottom panels) of (B) two rebastinib-treated *Krit1*$^{fl/fl}$; i*Pik3ca*^{H1047R} mice that developed significant CCM lesions by POD 21 and (C) one rebastinib-treated *Krit1*$^{fl/fl}$; i*Pik3ca*^{H1047R} mouse that showed no typical CCM pathology on POD 21. **(D)** Study flowchart outlining inclusion and exclusion criteria. **(E)** Representative microscopic images through the cranial windows (left panels) and visual images (right panels) of two vehicle-treated mice showing large lesion formation through cranial windows prior to study termination. **(F)** Serial of microscopic images through the cranial windows showing CCM growth in either vehicle- or rebastinib-treated mouse brains from POD 11 to POD 28. Two sets of representative microscopic images from this complete cohort are presented in Fig. 6 G to demonstrate the effects of rebastinib treatment in lesion burden. Scale bar: 1 mm.

Provided online are Table S1 and Table S2. Table S1 shows the list of primary and secondary antibodies used for western blot and immunofluorescence. Table S2 shows the list of gRNAs and siRNAs